Reviews in Mineralogy & Geochemistry
Vol. 55, pp. 197-230, 2004

The Isotope Geochemistry and Cosmochemistry of Magnesium

Edward D. Young
Department of Earth and Space Sciences
and
Institute of Geophysics and Planetary Physics
University of California Los Angeles
Los Angeles, California 90095-1567, U.S.A.

Albert Galy
Department of Earth Sciences
University of Cambridge
Cambridge, CB2 3EQ, United Kingdom

INTRODUCTION

Magnesium is second only to oxygen in abundance among the rock-forming elements and is an important element in the oceans and in hydrological and biological systems. Differences in the relative abundances of its three stable isotopes, ^{24}Mg (78.99%), ^{25}Mg (10.00%), and ^{26}Mg (11.01%), are expected as a result of physicochemical processes because of the large relative mass differences of 4 and 8% between ^{25}Mg and ^{26}Mg, and ^{24}Mg, respectively. Although isotopes of Mg have been used for many years as tracers in artificially spiked systems (in which the abundance of one isotope is enriched) (Cary et al. 1990; Dombovari et al. 2000), reliable measurements of ^{25}Mg/^{24}Mg and ^{26}Mg/^{24}Mg in natural systems have been limited historically by the 1‰ (one part per thousand) reproducibility imparted by instrumental mass fractionation effects. In order to be useful for many geochemical and cosmochemical applications the isotope ratios of Mg must be resolved to ≤200 parts per million (ppm). As a result, with a few exceptions (e.g., Davis et al. 1990; Goswami et al. 1994; Russell et al. 1998), many past studies of Mg isotope ratios focused on detection of non-mass dependent, so-called "anomalous" Mg isotopic effects rather than on investigations of mass-dependent fractionation. The principle outcome of this focus was the discovery of radiogenic ^{26}Mg (^{26}Mg*) in primitive meteorites (Gray and Compston 1974; Lee and Papanastassiou 1974).

With the advent of multiple-collector inductively coupled plasma-source mass spectrometry (MC-ICPMS) it is now possible to measure ^{25}Mg/^{24}Mg and ^{26}Mg/^{24}Mg of Mg in solution with a reproducibility of 30 to 60 ppm or better (Galy et al. 2001). What is more, ultraviolet (UV) laser ablation combined with MC-ICPMS permits *in situ* analysis of Mg-bearing mineral samples with reproducibility of 100 to 200 ppm (Young et al. 2002a). These new analytical capabilities allow mass-dependent fractionations of the isotopes of Mg to be used as tracers in natural systems.

Perhaps the greatest advance afforded by the MC-ICPMS technology is the ability to measure ^{25}Mg/^{24}Mg and ^{26}Mg/^{24}Mg independently with precision many times smaller than the magnitude of the natural variations. Thermal ionization mass spectrometry (TIMS)

1529-6466/04/0055-0006$05.00

methods provide highly precise measurements of anomalies in $^{26}Mg/^{24}Mg$ if the data are normalized to a fixed "terrestrial" $^{25}Mg/^{24}Mg$ value (the latter compensates for instrumental mass fractionation). The MC-ICPMS technique does not require $^{26}Mg/^{24}Mg$ measurements to be corrected to a single $^{25}Mg/^{24}Mg$. Instead, both ratios are measured with a high level of precision. For samples of purified Mg in solution the precision of the MC-ICPMS measurements is sufficient to resolve the various mass-dependent fractionation relationships that exist between the two isotope ratios. We are therefore on the threshold of establishing an entirely new aspect of isotope geo-cosmochemistry based on the details of the mass-dependent fractionations of Mg isotopes.

At this writing the number of published papers reporting high-precision Mg isotope ratios of natural materials is small but growing rapidly. Since Mg isotope geo-cosmochemistry is a young field, our goal in writing this review is to identify for the reader those areas that we view as ripe for future exploitation, especially with respect to the significance of the observed patterns of $^{25}Mg/^{24}Mg$ and $^{26}Mg/^{24}Mg$ variation in terrestrial and extraterrestrial reservoirs.

REFERENCE MATERIALS, NOMENCLATURE, AND ANALYTICAL CONSIDERATIONS

Reference material

The National Institute of Standards and Technology (NIST, formerly the National Bureau of Standards, or NBS) developed an isotopic standard for Mg (Catanzaro et al. 1966). The NIST Standard Reference Material 980, or SRM 980, is a magnesium metal certified for $^{25}Mg/^{24}Mg = 0.12663 \pm 0.00013$ (±1.0‰) and $^{26}Mg/^{24}Mg = 0.13932 \pm 0.00026$ (±1.9‰) (Catanzaro et al. 1966). The former value is universally adopted while the latter value has been questioned (Galy et al. 2001; Schramm et al. 1970). A more accurate value for $^{26}Mg/^{24}Mg$ may be 0.139828 ± 0.000037 (±0.27‰, 2σ), a full 3.6‰ greater than the accepted value (Galy et al. 2001).

A more pressing problem is that the SRM 980 reference material appears to be heterogeneous in its isotopic composition. The heterogeneity is found at the scale of individual metal chips (~10 mg), is entirely mass dependent, and is comparable in magnitude to the reported precision of the certified isotope ratios determined by TIMS (Galy et al. 2003). As a result, and despite the attractiveness of reporting isotope ratios relative to a recognized and certified standard, the SRM 980 metal is inappropriate for use as an isotope standard in high-precision work where differences of 0.2‰ or less are significant.

Virtually all of the published Mg isotope data obtained by MC-ICPMS are referenced to the SRM 980 standard at the time of this writing. Fortunately, the vast majority were obtained using as the standard a single batch of dissolved SRM 980 housed in the Department of Earth Sciences, University of Oxford. This standard has been referred to as SRM 980_O (Galy et al. 2003). However, SRM 980_O was never intended to serve as a primary standard and there is the need to establish an alternative primary standard of uniform composition.

A new standard has been developed in the Department of Earth Sciences, University of Cambridge (Galy et al. 2003). It consists of approximately 10 g of pure magnesium metal (provided by Dead Sea Magnesium Ltd., Israel) dissolved in a liter of 0.3 N HNO_3. This material, referred to as DSM3, is a suitable reference because it is already in solution and therefore immune to heterogeneity. In addition, it has the added advantage that its isotopic composition is indistinguishable from MC-ICPMS measurements of carbonaceous chondrite materials, a rational reference point with cosmochemical and petrological significance.

All of the data reported in this review have been converted from the SRM 980_O scale to the DSM3 scale (with the exception of data from several previously published figures).

This was done as a first step towards eliminating the confusion that will ensue if laboratories continue to report their results relative to the heterogeneous SRM 980 metal, and because the Mg isotopic compositions relative to DSM3 are effectively identical to values reported relative to "chondrite."

The definitions of $\delta^{25}Mg_{SRM\ 980\_O}$ and $\delta^{26}Mg_{SRM\ 980\_O}$ are:

$$\delta^{x}Mg^{sample}_{SRM\ 980\_O} = \left(\frac{(^{x}Mg/^{24}Mg)_{sample}}{(^{x}Mg/^{24}Mg)_{SRM\ 980\_O}} - 1 \right) 10^{3} \quad (1)$$

where *x* refers to either 25 or 26. From these values, conversion to the equivalent delta values on the DSM3 scale, $\delta^{25}Mg_{DSM3}$ and $\delta^{26}Mg_{DSM3,}$ is accomplished with the expression

$$\delta^{x}Mg^{sample}_{DSM3} = \delta^{x}Mg^{sample}_{SRM\ 980\_O} + \delta^{x}Mg^{SRM\ 980\_O}_{DSM3} + 0.001\,\delta^{x}Mg^{sample}_{SRM\ 980\_O}\ Mg^{SRM\ 980\_O}_{DSM3} \quad (2)$$

where

$$\delta^{25}Mg^{SRM\ 980\_O}_{DSM3} = -1.744 \quad (3)$$

and

$$\delta^{26}Mg^{SRM\ 980\_O}_{DSM3} = -3.405 \quad (4)$$

The values for the SRM 980_O relative to DSM3 are reported by Galy et al. (2003). The 0.001 factor arises when converting sample/standard ratios from one standard to another in δ notation.

Nomenclature

Early studies of Mg isotope ratios in geological materials used the notation $\Delta^{25}Mg$ to mean per mil deviations from a standard as expressed in Equation (1) above, a convention that persists today (e.g., Hsu et al. 2000). The values assigned to $\Delta^{25}Mg$ in those studies represent the level of mass-dependent isotopic fractionation relative to the standard. The same convention defined $\delta^{26}Mg$ as the per mil deviation from the standard after correction for the mass fractionation evidenced by $\Delta^{25}Mg$. In this system of nomenclature, Δ values refer to *mass dependent fractionations* while δ values refer to deviations from mass-dependent fractionation (i.e., the $\delta^{26}Mg$ defines excesses in ^{26}Mg relative to mass fractionation attributable to decay of the extinct nuclide ^{26}Al). In some cases $\Delta^{25}Mg$ has been replaced by the symbol F_{Mg} (Kennedy et al. 1997) where the F refers to "fractionation."

The nomenclature described above is common in the cosmochemistry literature for not only Mg but other systems as well (e.g., Ti; Fahey et al. 1987). It arose because naturally-occurring mass fractionation effects and instrumental effects were convolved and not easily distinguished. Instead it was the deviations from mass fractionation (i.e., nucleosynthetic effects) that were the primary focus. However, beginning with McKinney et al. (1950) the symbol δ has been used in the terrestrial literature to mean per mil deviations from a standard in the O, C, S, N, and D/H isotope systems. In this context the use of δ has no connotation with respect to the distinction between mass dependent and non-mass dependent fractionation. Following the discovery of non-mass dependent effects in oxygen in both extraterrestrial and terrestrial materials, the capital delta Δ became ensconced as the symbol that quantifies *deviation from mass-dependent fractionation* in that system. In the oxygen system $\Delta^{17}O$ refers to the intercept on a plot of $\delta^{17}O$ (ordinate) against $\delta^{18}O$ (abscissa) and $\delta^{17}O$ and $\delta^{18}O$ refer to per mil deviations in $^{17}O/^{16}O$ and $^{18}O/^{16}O$ from a standard (usually Standard Mean Ocean Water). Accordingly to this definition, $\Delta^{17}O$ should not change significantly with mass-

dependent fractionation (within <0.3‰), although in detail small differences are expected (Young et al. 2002b). On the other hand, large differences in $\Delta^{17}O$ serve as indication that there are departures from mass-dependent fractionation. Similarly, sulfur is also now known to experience non-mass dependent fractionation and as a consequence $^{33}S/^{32}S$ and $^{34}S/^{32}S$ are reported as per mil deviations from a standard using $\delta^{33}S$ and $\delta^{34}S$ and $\Delta^{33}S$ is used, by analogy with $\Delta^{17}O$, as a measure of departure from mass-dependent fractionation curves in $\delta^{33}S$ vs. $\delta^{34}S$ space.

With regard to Mg isotopes, one is therefore forced to choose between the merit of precedence in the cosmochemistry community and that of conformity with the other light stable isotope systems when deciding upon a nomenclature for reporting $^{25}Mg/^{24}$ and $^{26}Mg/^{24}Mg$ data. We have chosen to come down on the side of conformity with the other light element isotope systems and will use $\delta^{25}Mg$ and $\delta^{26}Mg$ (defined in Eqn. 1) to mean simply the per mil deviations from a standard (usually DSM3). In keeping with the nomenclature of other stable isotope systems, $\Delta^{25}Mg$ is defined as the intercept on a plot of $\delta^{25}Mg$ (ordinate) vs. $\delta^{26}Mg$ (abscissa). A more precise definition of $\Delta^{25}Mg$ will be presented in the following section. The symbol $\delta^{26}Mg^*$ can then be reserved for deviations from mass fractionation attributable to $^{26}Mg^*$, consistent with the definition in many existing cosmochemistry papers.

We strongly recommend that these conventions be adopted at this early stage in the development of Mg isotope geochemistry and cosmochemistry to eliminate the current ambiguity in the meaning of the Δ symbol in the literature. Presumably, confusion will be kept to a minimum if the same meaning is assigned to the same symbols in different isotope systems where ever possible.

Analytical considerations

High-precision Mg isotope ratios can now be obtained by MC-ICPMS because instrumental fractionation (α_{inst}) can be precisely monitored. MC-ICPMS measurements of Mg isotope ratios are obtained by measuring ^{24}Mg, ^{25}Mg and ^{26}Mg signals simultaneously on three Faraday cup collectors. When using low-mass-resolution Ar-ICP-source mass spectrometers, the Mg mass spectrum can include spectral (i.e., isobaric) interferences. Potential interfering species include $^{48}Ti^{++}$, $^{50}Ti^{++}$, $^{48}Ca^{++}$, $^{50}Cr^{++}$, $^{52}Cr^{++}$, CN^+, CC^+ and various hydrides (e.g., C_2H^+). The H-bearing molecules, including Mg-hydride, become negligible in dry plasmas (Galy et al. 2001; Young et al. 2002a). The effects of N, although ubiquitous, can be rendered negligible by avoiding N_2 gas as an augmentation to Ar in the desolvating nebulizers. Effects of the other elements can be removed by measuring pure solutions of Mg (e.g., Chang et al. 2003). When purification is not possible the effects of the interfering species can be mitigated by matching analyte signal intensities. For laser ablation studies, interference effects must be determined in advance or monitored as part of the analytical scheme (e.g., Young et al. 2002a).

Higher mass resolution is becoming more common in MC-ICPMS technology. The result will be a reduction in the hindrances of isobaric interferences. With judicious use of narrow entrance slits and improvements in ion optics, even smaller radius instruments can resolve $^{50}Ti^{++}$ from $^{25}Mg^+$, for example. However, at this writing most studies have made use of low-mass-resolution instruments, and even with high mass resolution, care must still be taken to avoid changes in instrumental fractionation due the presence of elements other than the analyte in the plasma.

Solutions. Correction for α_{inst} is most often made using a standard-sample bracketing technique (e.g., Galy et al. 2001). In this protocol, standard and sample isotope ratios obtained by multiple measurement cycles are compared and the sample result expressed as a deviation from the standard. Cross contamination between the sample and the standard is avoided by washing the analytical instrumentation with dilute (usually about 0.1N) HNO_3 for several minutes between analyses. Introduction of Mg in dilute HNO_3 (e.g., 0.1N) into the MC-ICPMS

via a desolvating nebulizer reduces O, N, C and H spectral interferences to an insignificant level. In addition, concentrations of Mg in the standard and the sample can be kept within 25% of each other to further minimize the potential influences of isobaric interferences.

Impure solutions of common minerals can induce isotopic biases of up to 0.5‰ per atomic mass unit (amu) (e.g., Galy et al. 2001). These so-called matrix effects are mass-dependent and are the result of changes in α_{inst}. Shifts in $\alpha_{inst.}$ are most sensitive to the presence of Ca and K followed by Zn, Al and Na. The matrix effect caused by the presence of Fe in solution is apparently less severe (Galy et al. 2001; Galy et al. in review). High precision and accuracy can still be obtained on multi-element solutions but only when the chemistry of the sample is identical to the chemistry of the standard. For accurate results, chemical purification is advisable. Chemical separation of Mg can be accomplished by liquid chromatographic methods but these introduce a mass-dependent isotopic fractionation of 1.25‰ per amu between the first and last 10% fractions (Chang et al. 2003). The preferred method makes use of Bio-Rad AG50W-X12 ion exchange resin through which >99% recovery of Mg is achieved (Galy et al. 2002; Chang et al. 2003). The size of the matrix effect related to alkali elements and Ca implies that [K+Ca+Na]/[Mg] must be lower than 0.05 (mol ratios) if the inaccuracy related to matrix effect is to be lower than the long term external reproducibility of the method. Therefore, K, Na and Ca blank levels in the eluent and acid used are the limiting factor of the sensitivity and accuracy of the method.

Laser ablation. Instrumental mass fractionation is generally accounted for in laser ablation analyses of Mg isotope ratios using sample-standard bracketing. The standard can be either a solid or a solution. The material liberated by laser ablation includes all of the elements comprising the target. As a result, investigations into the possible spectral interferences attributable to these elements are required. Young et al. (2002a) found that the interference effects of Ca and Ti were negligible for many minerals including Mg-rich olivine, clinopyroxene, Al-Ti-rich clinopyroxene, melilite, and spinel. For example, the concentration of Ca sufficient to bias measured magnesium isotope ratios was determined empirically by aspirating solutions of 1 to ~200 ppm Ca in dilute HNO_3 through the desolvating nebulizer and into the sample carrier gas during laser ablation of a standard consisting of a grain of forsterite. Because the mass resolution was too low to resolve $^{48}Ca^{++}$ and $^{24}Mg^{+}$, $^{44}Ca^{++}$ was used as a proxy for $^{48}Ca^{++}$ in order to calculate the amount of $^{48}Ca^{++}$ entering the source. Measurable interference on m/z = 24 signals due to the presence of $^{48}Ca^{++}$ occurred when the concentrations of Ca reaching the plasma source were sufficient to produce $^{44}Ca^{++}/^{24}Mg^{+}$ voltage ratios >1‰. This limit could then be used as a criterion for assessing the accuracy of analyses of unknowns that contain both Ca and Mg.

The "matrix effects" attributable to Fe, Ti, Al, Na, and K during laser ablation analyses of Mg isotope ratios have been investigated (Young et al. 2002a; Norman et al. 2004). Results indicate that these elements do not influence measured Mg isotope ratios at the 0.1‰ per amu level of detection for most common rock-forming minerals in which Mg is a significant component. However, effects greater than 1‰ have been observed when analyzing Mg as a minor element in feldspar and more work will be required to assess the accuracy obtainable by laser ablation of minerals containing small concentrations of Mg.

Matrix effects on measured Mg isotope ratios due to the presence of Fe in laser ablation targets require further study. Young et al. (2002a) found that adding Fe via solution to the plasma to yield $^{56}Fe^{+}/^{24}Mg^{+}$ up to 2.0 resulted in no measurable shifts in $^{25}Mg/^{24}Mg$ and $^{26}Mg/^{24}Mg$ of laser ablation products. Norman et al. (2004) showed that there is a shift in instrumental fractionation in measured $^{25}Mg/^{24}Mg$ on the order of +0.06‰ for every 1% decrease in Mg/(Mg+Fe) of the olivine target. These disparate results might be explained by ionization in different locations in the torch when samples are introduced by aspiration of solutions rather than by gas flow from a laser ablation chamber. Different matrix effects for solutions and laser

ablation products will depend on the details of the instrument configuration, including the status of the guard electrode, sample load, and radio frequency power.

Inspection of ultraviolet laser ablation pits by backscattered electron imaging, micro-Raman spectroscopy, and characteristic X-ray analysis shows that extraction of the material from the laser pits is quantitative (Young et al. 2002a). Fractionation due to the laser sampling process must arise therefore from incomplete transfer of material after ablation rather than as a result of the ablation itself. Years of experience with UV laser ablation has shown that elemental and isotopic fractionation is minimized by ablating in an atmosphere of He (rather than Ar). The He gas permits the plasma plume that extends above the ablation pit to expand freely, enhancing entrainment into the carrier gas stream. An Ar makeup gas is added to the He flow prior to entering the plasma of the ICPMS in order to "punch" the sample into the torch. Studies to date indicate that fractionation attributable to transport of ablated materials is reproducible since accurate results (as compared with results from solutions of purified Mg) are obtained for a variety of mineral materials using sample-standard bracketing methods.

MAGNESIUM ISOTOPE RESERVOIRS

High-precision values of δ^{26}Mg for Mg obtained by acid digestion of bulk samples, purification of the analyte Mg (Galy et al. 2001), and analysis of dilute acid solutions of the extracted Mg are available for several meteorite samples, mineral grains from mantle nodules, a sample of loess from China representing continental crust, continental basalts, seawater, foraminifera, various carbonate rocks, speleothems and their associated waters, Mg metals, magnesia, and even spinach chlorophyl. These high-precision analyses are shown in Figure 1 and tabulated in Table 1.

Whole rock samples of CI meteorite, matrix of LL3 meteorite, and clinopyroxene from a single mantle nodule are indistinguishable from the DSM3 standard and suggest that δ^{26}Mg = 0.0‰ is a reasonable estimate of the chondritic reservoir for Mg (Galy and O'Nions 2000). Young et al. (2002a) report an analysis of olivine from the same sample of mantle nodule that is 0.8‰ lower in δ^{26}Mg than the clinopyroxene shown here. There is concern that this sample of olivine may have been altered. The olivine value has been verified using laser ablation several times on different instruments (Young et al. 2002a; unpub.) but the possibility for cryptic alteration remains and the olivine analysis may not be representative of mantle values.

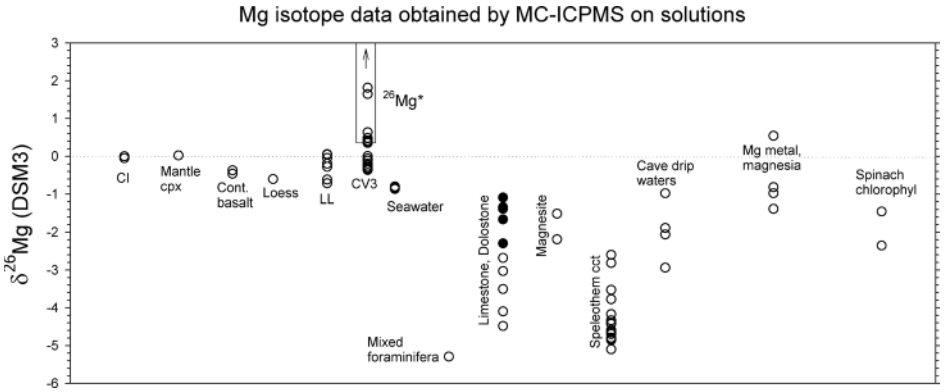

Figure 1. Compilation of δ^{26}Mg values (relative to DSM3) for various terrestrial and extraterrestrial reservoirs. Data and sources are tabulated in Table 1. For the carbonates, the black points represent dolomite while the open symbols represent calcite.

Table 1. Mg isotope ratios determined by MC-ICPMS analysis of purified Mg in weak acid solution. Three significant figures are shown to aid in the calculation of $\Delta^{25}Mg'$ values.

Sample	Source	$\delta^{26}Mg$	±2σ	$\delta^{25}Mg$	±2σ
Metal and oxide					
SRM 980 Mg metal	1	−3.405	0.07	−1.744	0.04
Romil Mg metal	1	−0.977	0.086	−0.508	0.049
Aldrich Mg metal	1	−0.816	0.172	−0.416	0.082
Dead Sea Mg metal	1	0.543	0.150	0.279	0.079
Petzl's magnesie	1	−1.383	0.042	−0.716	0.013
Organic matter					
Spinach chlorophyll (b)	1	−2.349	0.067	−1.204	0.026
Spinach chlorophyll (a)	1	−1.451	0.098	−0.741	0.062
Carbonate					
Magnesite, Piemont, Italy	1	−2.186	0.044	−1.146	0.035
Magnesite, Transvaal, South Africa	1	−1.508	0.143	−0.768	0.076
Dolomite	2	−1.771	0.040	−0.865	0.010
Dolostone, MSR	3	−1.089	0.036	−0.555	0.016
Dolostone, SR-D-1	3	−2.290	0.096	−1.184	0.033
Dolostone LH	3	−1.382	0.082	−0.710	0.108
Dolostone LH, AP867	3	−1.339	0.190	−0.676	0.094
Dolostone LH AP865	3	−1.660	0.119	−0.847	0.055
Marble TSS NL251	3	−3.496	0.036	−1.828	0.039
Marble TSS NL252	3	−2.676	0.018	−1.375	0.062
Marble TSS XP210	3	−3.024	0.076	−1.583	0.041
Limestone (Cen), PEK-HOST	3	−4.088	0.072	−2.123	0.003
Limestone (Tur), DDC	3	−4.472	0.015	−2.328	0.026
Speleothem, SR-2N-F	3	−4.628	0.115	−2.400	0.070
Speleothem, SR-2N-K	3	−4.623	0.083	−2.391	0.043
Speleothem SR-2-10-C1	3	−4.780	0.029	−2.465	0.019
Speleothem SR-2-10-C2	3	−4.820	0.001	−2.492	0.006
Speleothem SR-2-10-C2	3	−4.840	0.040	−2.498	0.045
Speleothem SR-2-10-D1	3	−4.826	0.022	−2.491	0.020
Speleothem SR-5-3-00-S	3	−4.636	0.116	−2.392	0.028
Speleothem SR-8-5-00-S	3	−4.617	0.019	−2.393	0.031
Speleothem SR-13-3-00-S	3	−2.594	0.025	−1.338	0.010
Spleothem, SR-2-8-B	3	−4.414	0.120	−2.282	0.065
Spleothem, SR-2-8-E3	3	−4.158	0.106	−2.154	0.074
Speleothem, SR-2-8-J	3	−4.579	0.126	−2.372	0.089
Speleothem, SR-2-8-G	3	−4.685	0.122	−2.414	0.027
Mixed-species foraminifera tests	2	−5.279	0.160	−2.732	0.100
Water					
Drip water, SR-5-3-00-W	3	−1.884	0.066	−0.965	0.034
Drip water, SR-8-5-00-W	3	−2.057	0.028	−1.048	0.060
Drip water, SR-13-3-00-W	3	−2.931	0.020	−1.500	0.047
Ground water, Har-Tuv4	3	−1.696	0.056	−0.870	0.014
Drip water, MSS	3	−0.975	0.057	−0.492	0.055
Drip water, TDGW	3	−2.433	0.119	−1.277	0.048
North Atlantic seawater	2	−0.824	0.040	−0.416	0.080
Mediterranean water	4	−0.864	0.122	−0.434	0.105
Atlantic seawater (SWOM)	4	−0.799	0.037	−0.407	0.007
Mediterranean surface water	4	−0.851	0.244	−0.422	0.121

Table continued on next page.

Table 1. *(continued from previous page)*

Sample	Source	δ^{26}Mg	±2σ	δ^{25}Mg	±2σ
Terrestrial silicate					
Continental basalt BR	4	−0.460	0.185	−0.250	0.047
Continental basalt BCR-1	4	−0.368	0.105	−0.186	0.070
Mantle nodule clinopyroxene Jl-1	5	0.022	0.093	0.017	0.073
Mantle nodule olivine Jl-1	5	−1.093	0.117	−0.558	0.096
Loess, China	4	−0.602	0.222	−0.308	0.148
Allende Meteorite (CV3)					
chondrule AG38	6	−0.333	0.092	−0.178	0.039
chondrule AG67II	6	−0.060	0.027	−0.027	0.015
chondrule A2	6	0.354	0.134	0.186	0.071
chondrule A3	6	−0.248	0.064	−0.118	0.056
chondrule A4	6	1.648	0.080	0.737	0.069
chondrule A5	6	0.487	0.053	0.223	0.085
chondrule A6	6	0.381	0.115	0.198	0.060
chondrule A7	6	−0.252	0.034	−0.118	0.018
chondrule A8	6	−0.362	0.113	−0.176	0.038
chondrule AH3	6	−0.192	0.043	−0.087	0.021
chondrule AH2	6	1.818	0.020	0.864	0.020
chondrule AH1	6	0.420	0.040	0.189	0.001
chondrule AH4	6	0.639	0.031	0.291	0.046
chondrule A9, rim	6	−0.116	0.043	−0.060	0.015
chondrule A9, core	6	0.009	0.042	0.004	0.028
CAI, AG178	6	11.917	0.024	5.117	0.005
Whole rock	6	−0.300	0.073	−0.160	0.031
Matrix	6	−0.287	0.044	−0.151	0.009
Bjurbole Meteorite (L/LL4)					
chondrule AG162	7	−0.194	0.159	−0.082	0.069
chondrule AG163	7	−0.275	0.043	−0.145	0.029
chondrule AG164	7	−0.714	0.068	−0.340	0.020
Orgueil Meteorite (CI)					
Whole rock, AG94	8	0.003	0.060	0.002	0.048
Whole rock, AG95	8	−0.050	0.079	−0.015	0.045
Chainpur Meteorite (LL3)					
Matrix, AG76	4	0.059	0.093	0.050	0.025
Matrix, AG77	4	0.046	0.110	0.023	0.066
Chondrule C11	4	−0.615	0.079	−0.307	0.043
Chondrule C12	4	−0.045	0.131	−0.027	0.062
Evaporation products					
chondrule AH3, re-melted	7	6.741	0.001	3.450	0.006
chondrule AG162, re-melted	7	0.861	0.060	0.459	0.014
chondrule AG163, re-melted	7	5.215	0.040	2.676	0.030
chondrule AG164, re-melted	7	0.899	0.227	0.472	0.107

Sources: (1) Galy et al. 2001; (2) Chang et al. 2003; (3) Galy et al. 2002; (4) This study; (5) Young et al. 2002; (6) Galy et al. 2000; (7) Young et al. 2002; (8) Galy et al. in press

Support for this conclusion comes from laser ablation analyses of mantle olivines recently reported by Norman et al. (2004). The loess and continental basalt samples suggest that evolved crustal materials may be on average approximately 0.4–0.6‰ lower in δ^{26}Mg than the primitive CI/mantle reservoir (Fig. 1).

Chondrules from Chainpur LL3 meteorite have somewhat lower δ^{26}Mg values than Chainpur LL3 matrix, CI, and terrestrial mantle clinopyroxene. Chondrules from the Bjurbole L/LL4 ordinary chondrite also have slightly lower δ^{26}Mg values than CI and LL3 matrix. Chondrules, matrix, and whole rock samples from the Allende CV3 meteorite span a larger range in δ^{26}Mg that overlaps the CI and ordinary chondrite data.

The CV3 δ^{26}Mg values greater than approximately 0.5‰ on the DSM3 scale reflect the presence of radiogenic ^{26}Mg (^{26}Mg *) formed by β+ decay of extinct ^{26}Al (half life = 0.72 m.y.). The origin of the ^{26}Mg* in the chondrules will be discussed further in the sections on extraterrestrial materials. Not shown in Figure 1 is a bulk CAI sample that has a δ^{26}Mg value of 11.85‰. This latter value reflects both mass fractionation and ^{26}Mg*. Excluding the ^{26}Mg*-bearing samples, the Allende data define a narrow spread in δ^{26}Mg values of about 1‰. The significance of the variability in δ^{26}Mg among the ^{26}Mg*-bearing samples and the uniformity in δ^{26}Mg among the ^{26}Mg*-free samples is discussed in sections describing the meteorite data that follow.

Carbonate rocks and foraminifera tests (a sample of mixed species) are consistently lower in δ^{26}Mg than Mg from seawater by several per mil. In addition, Mg in calcite is consistently lower in δ^{26}Mg than Mg in dolomite by approximately 2‰ (Fig. 1). These data together with the samples of coeval speleothem calcite and waters show that the heavy isotopes of Mg partition to water relative to carbonate minerals. In this respect the Mg isotopes behave much like the isotopes of Ca (Gussone et al. 2003; Schmitt et al. 2003). There is not yet sufficient data to assess with confidence the temperature dependence of the fractionation of Mg isotopes between carbonates and waters, although Galy et al. (2002) concluded that the evidence so far is that temperature effects are below detection in the range 4–18°C.

In summary, there is a clear mineralogical control on the partitioning of the Mg isotopes among carbonates and waters and, apparently, a weak dependence on temperature at low *T*. An important question is the extent to which these measured values for carbonates and waters reflect isotopic equilibrium. Hints to the answer come from comparing δ^{26}Mg to δ^{25}Mg, as shown in the section on terrestrial reservoirs.

Kinetic, or "vital," isotopic effects may be evidenced in the samples of mixed foraminifera and seawater reported by Chang et al. (2003). Again, the relationship between δ^{26}Mg and δ^{25}Mg help answer this question (see below), although the data are too few to reach firm conclusions at this stage.

On a standard plot of δ^{25}Mg vs. δ^{26}Mg all of the terrestrial data follow the expected mass-fractionation trends (Fig. 2). Deviations from mass fractionation are evident in several of the meteorite samples. The details of the relationships between δ^{25}Mg vs. δ^{26}Mg are the subject of several following sections.

RESOLVING MECHANISMS OF ISOTOPE FRACTIONATION WITH THREE ISOTOPE DIAGRAMS

The mass-dependent fractionation laws that describe the partitioning of three or more isotopes are different for kinetic and equilibrium reactions. The precision with which Mg isotope ratios can be measured by MC-ICPMS is sufficient to take advantage of these differences. Relationships between ^{25}Mg/^{24}Mg and ^{26}Mg/^{24}Mg are diagnostic of kinetic

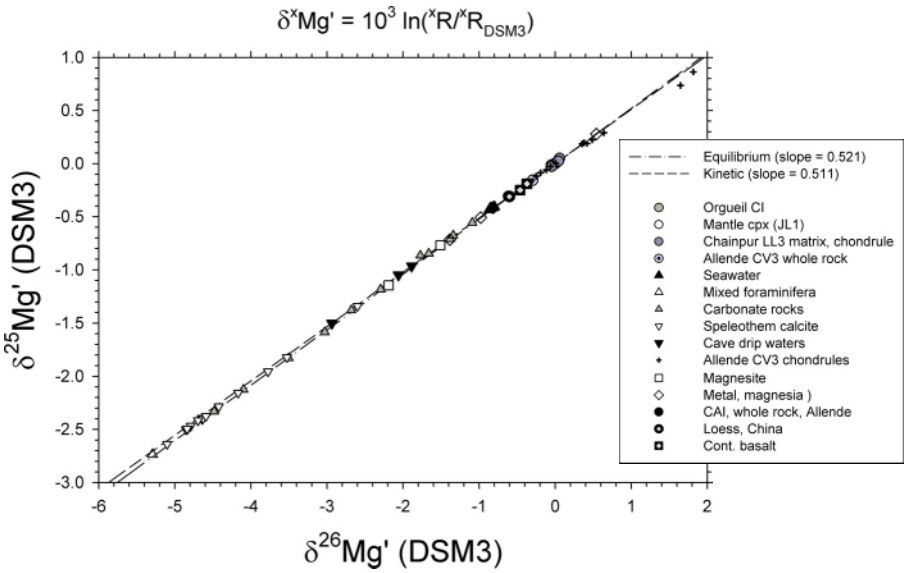

Figure 2. Magnesium three-isotope plot showing terrestrial and extraterrestrial samples relative to the predicted equilibrium and kinetic mass fractionation laws. The slopes in the caption refer to the β values that characterize the mass fractionation laws.

fractionation, equilibrium fractionation, and, in the case of extraterrestrial samples, even subtle departures from both. The theory and methods for applying this new technique to the Mg isotope system are described below.

Mass-dependent fractionation laws

The fractionation laws relating two or more isotope ratios are described by a relationship between the fractionation factors for the isotope ratios. Using Mg as an example, the three isotopes ^{24}Mg, ^{25}Mg, and ^{26}Mg define two fractionation factors

$$\alpha_{25/24} = \frac{(^{25}\mathrm{Mg}/^{24}\mathrm{Mg})_a}{(^{25}\mathrm{Mg}/^{24}\mathrm{Mg})_b} \tag{5}$$

and

$$\alpha_{26/24} = \frac{(^{26}\mathrm{Mg}/^{24}\mathrm{Mg})_a}{(^{26}\mathrm{Mg}/^{24}\mathrm{Mg})_b} \tag{6}$$

where *a* and *b* refer to either two different conditions or two different materials. At equilibrium the two fractionation factors are related by the expression

$$\frac{\ln\alpha_{25/24}}{\ln\alpha_{26/24}} = \frac{\left(\frac{1}{m_1} - \frac{1}{m_2}\right)}{\left(\frac{1}{m_1} - \frac{1}{m_3}\right)} \tag{7}$$

where m_1 is the atomic mass of ^{24}Mg (23.985042), m_2 is the atomic mass of ^{25}Mg (24.985837), and m_3 is the atomic mass of ^{26}Mg (25.982593) (Hulston and Thode 1965; Matsuhisa et al. 1978; Weston 1999; Young et al. 2002b). Equation (7) can be rearranged to give

$$\alpha_{25/24} = \left(\alpha_{26/24}\right)^{\beta} \tag{8}$$

where the exponent is

$$\beta = \frac{\left(\frac{1}{m_1} - \frac{1}{m_2}\right)}{\left(\frac{1}{m_1} - \frac{1}{m_3}\right)} \tag{9}$$

Equation (9) is a high-temperature limit for the exponent in the equilibrium fractionation law that is a good indication of the true equilibrium value (Young et al. 2002b). The value for the exponent obtained from the atomic masses of the Mg isotopes is 0.5210.

Kinetic isotope fractionation obeys a different fractionation law. Young et al. (2002b) showed recently that kinetic processes, again written here in terms of the two Mg isotope fractionation factors, obey the relation

$$\frac{\ln \alpha_{25/24}}{\ln \alpha_{26/24}} = \frac{\ln\left(\frac{M_1}{M_2}\right)}{\ln\left(\frac{M_1}{M_3}\right)} \tag{10}$$

where M_1, M_2, and M_3 are the masses in motion associated with the kinetic process. As before, Equation (10) can be rewritten as

$$\alpha_{25/24} = \alpha_{26/24}{}^{\beta} \tag{11}$$

where the exponent β is no longer given by Equation (9) but is instead

$$\beta = \frac{\ln\left(\frac{M_1}{M_2}\right)}{\ln\left(\frac{M_1}{M_3}\right)} \tag{12}$$

The masses in the kinetic β will be reduced masses if the rate limiting step involves vibrations (as during bond rupture), they will be molecular masses of isotopomers if the kinetic process involves transport of molecules, and they will be atomic masses if transport of atoms is involved. The value of the kinetic β goes down as the masses in (12) increase. As a result, an estimate of the maximum value for β during the kinetic fractionation of Mg isotopes is obtained by equating the M_i values with the atomic masses of Mg. The kinetic β obtained from the atomic masses of Mg is 0.5110.

In summary, the different mass-dependent fractionation laws that relate the two fractionation factors for the Mg isotopes are characterized by the value for β in the expression $\alpha_{25/24} = (\alpha_{26/24})^{\beta}$. For equilibrium processes β should be close to 0.521. For kinetic processes involving Mg atoms β should be close to 0.511.

Mass-fractionation in three-isotope space

The equilibrium and kinetic fractionation laws

$$\alpha_{25/24} = (\alpha_{26/24})^{\beta} \tag{13}$$

define curves on plots of δ^{25}Mg vs. δ^{26}Mg. These "mass fractionation curves" follow the general equation

$$\delta^{25}\mathrm{Mg} = (10^3 + \delta^{25}\mathrm{Mg}_{\mathrm{ref}})\left(\frac{10^3 + \delta^{26}\mathrm{Mg}}{10^3 + \delta^{26}\mathrm{Mg}_{\mathrm{ref}}}\right)^{\beta} - 10^3 \tag{14}$$

In this equation the reference composition (designated by the ref subscript) lies on the fractionation curve and might be, for example, the initial composition for an array of fractionated samples. All of the δ values in the equation refer to the same standard (e.g., DSM3) but this standard need not be on the fractionation curve itself (in other words, the fractionation curves described by Equation (14) do not have to pass through the origin on a plot of δ^{25}Mg vs. δ^{26}Mg).

One way to compare data to predicted fractionation laws is to plot the data on the three isotope plot in which δ^{25}Mg is the ordinate and δ^{26}Mg is the abscissa, and examine how closely the data fall to the different curves defined by the exponent β. However, the differences between the different β values are often evident only with careful attention to the statistics of the data. Ideally, the values of β should be obtained by a best fit to the data. This is most easily accomplished if the problem can be rewritten so that β is the slope in a linear regression.

Hulston and Thode (1965) showed that the relationship between δ values on a three isotope plot can be made linear if the definition of the δ's are modified so that the term $({}^{x}R/{}^{x}R_{std} - 1)$ is replaced by $\ln({}^{x}R/{}^{x}R_{std})$ where *x* refers to one of the minor isotopes, *R* is the ratio of the minor isotope to the major isotope and *std* refers to the standard ratio. In the case of Mg isotopes, the new definitions for δ^{25}Mg′ and δ^{26}Mg′ are:

$$\delta^{x}\mathrm{Mg}' = \ln\left(\frac{({}^{x}\mathrm{Mg}/{}^{24}\mathrm{Mg})_{\mathrm{sample}}}{({}^{x}\mathrm{Mg}/{}^{24}\mathrm{Mg})_{\mathrm{DSM3}}}\right)10^3 \tag{15}$$

where *x* refers to either 25 or 26. The fractionation curves written in terms of these new, linearized δ′ values are straight lines of the form

$$\delta^{25}\mathrm{Mg}' = \beta\,\delta^{26}\mathrm{Mg}' - \beta\,\delta^{26}\mathrm{Mg}'_{\mathrm{ref}} - \delta^{25}\mathrm{Mg}'_{\mathrm{ref}} \tag{16}$$

where the slope is the exponent β and the intercept is determined by the reference composition (if the reference composition is DSM3, then the intercept is the origin) .

When the Mg isotope data are cast in terms of the new δ′ values, they can be subjected to well-established linear regression techniques to extract the best-fit exponent β. A handy equation that converts the original δ values to the new, linear δ′ values is

$$\delta' = 10^3 \ln\left(\frac{(\delta + 10^3)}{10^3}\right) \tag{17}$$

The linear δ′ values for the data from Table 1 are shown in Table 2.

By plotting the highly precise Mg isotope data collected by MC-ICPMS in terms of δ^{25}Mg′ vs. δ^{26}Mg′ (Table 2) it is possible to constrain the values for β from the best-fit slopes defined by the data and therefore the nature of the fractionation processes that lead to the distribution of data. This method is applied in sections below.

Table 2. Mg isotope ratios determined by MC-ICPMS analysis of purified Mg in weak acid solution expressed in terms of linear delta values.

Sample	Source	$\delta^{26}Mg'$	$\delta^{25}Mg'$	$\Delta^{25}Mg'$
Metal and oxide				
SRM 980 Mg metal	1	−3.415	−1.746	0.033
Romil Mg metal	1	−0.978	−0.509	0.001
Aldrich Mg metal	1	−0.816	−0.416	0.009
Dead Sea Mg metal	1	0.543	0.279	−0.004
Petzl's magnesie	1	−1.384	−0.716	0.005
Organic matter				
Spinach chlorophyll (b)	1	−2.352	−1.204	0.021
Spinach chlorophyll (a)	1	−1.452	−0.742	0.015
Carbonate				
Magnesite, Piemont, Italy	1	−2.189	−1.146	−0.006
Magnesite, Transvaal, South Africa	1	−1.509	−0.768	0.018
Dolomite	2	−1.772	−0.866	0.057
Dolostone, MSR	3	−1.090	−0.556	0.012
Dolostone, SR-D-1	3	−2.293	−1.185	0.010
Dolostone LH	3	−1.383	−0.711	0.010
Dolostone LH, AP867	3	−1.340	−0.676	0.022
Dolostone LH AP865	3	−1.661	−0.847	0.018
Marble TSS NL251	3	−3.502	−1.829	−0.005
Marble TSS NL252	3	−2.680	−1.376	0.020
Marble TSS XP210	3	−3.028	−1.585	−0.007
Limestone (Cen), PEK-HOST	3	−4.096	−2.126	0.009
Limestone (Tur), DDC	3	−4.482	−2.331	0.004
Speleothem, SR-2N-F	3	−4.638	−2.403	0.013
Speleothem, SR-2N-K	3	−4.634	−2.394	0.021
Speleothem SR-2-10-C1	3	−4.792	−2.468	0.029
Speleothem SR-2-10-C2	3	−4.832	−2.495	0.023
Speleothem SR-2-10-C2	3	−4.852	−2.501	0.027
Speleothem SR-2-10-D1	3	−4.837	−2.494	0.026
Speleothem SR-5-3-00-S	3	−4.647	−2.395	0.027
Speleothem SR-8-5-00-S	3	−4.627	−2.396	0.015
Speleothem SR-13-3-00-S	3	−2.598	−1.339	0.015
Spleothem, SR-2-8-B	3	−4.424	−2.285	0.020
Spleothem, SR-2-8-E3	3	−4.167	−2.156	0.015
Speleothem, SR-2-8-J	3	−4.590	−2.375	0.016
Speleothem, SR-2-8-G	3	−4.696	−2.416	0.030
Mixed-species foraminifera tests	2	−5.293	−2.736	0.021
Water				
Drip water, SR-5-3-00-W	3	−1.886	−0.965	0.017
Drip water, SR-8-5-00-W	3	−2.059	−1.049	0.024
Drip water, SR-13-3-00-W	3	−2.935	−1.501	0.028
Ground water, Har-Tuv4	3	−1.698	−0.870	0.014
Drip water, MSS	3	−0.975	−0.492	0.016
Drip water, TDGW	3	−2.436	−1.277	−0.008
North Atlantic seawater	2	−0.824	−0.416	0.013
Mediterranean water	4	−0.864	−0.434	0.016
Atlantic seawater (SMOW)	4	−0.800	−0.407	0.010
Mediterranean surface water	4	−0.852	−0.422	0.022

Table continued on next page.

Table 2. *(continued from previous page)*

Sample	Source	$\delta^{26}Mg'$	$\delta^{25}Mg'$	$\Delta^{25}Mg'$
Terrestrial silicate				
Continental basalt BR	4	−0.460	−0.250	−0.010
Continental basalt BCR-1	4	−0.368	−0.186	0.005
Mantle nodule clinopyroxene Jl-1	5	0.022	0.017	0.006
Mantle nodule olivine Jl-1	5	−1.094	−0.558	0.012
Loess, China	4	−0.602	−0.308	0.006
Allende Meteorite (CV3)				
chondrule AG38	6	−0.333	−0.178	−0.004
chondrule AG67II	6	−0.060	−0.027	0.004
chondrule A2	6	0.354	0.186	0.002
chondrule A3	6	−0.248	−0.118	0.011
chondrule A4	6	1.646	0.737	−0.121
chondrule A5	6	0.487	0.223	−0.031
chondrule A6	6	0.381	0.197	−0.001
chondrule A7	6	−0.252	−0.118	0.013
chondrule A8	6	−0.362	−0.176	0.012
chondrule AH3	6	−0.192	−0.087	0.013
chondrule AH2	6	1.817	0.863	−0.083
chondrule AH1	6	0.420	0.189	−0.030
chondrule AH4	6	0.639	0.291	−0.042
chondrule A9, rim	6	−0.116	−0.060	0.000
chondrule A9, core	6	0.009	0.004	−0.001
CAI, AG178	6	11.847	5.104	−1.068
Whole rock	6	−0.300	−0.160	−0.003
Matrix	6	−0.287	−0.151	−0.002
Bjurbole Meteorite (L/LL4)				
chondrule AG162	7	−0.194	−0.082	0.019
chondrule AG163	7	−0.275	−0.145	−0.002
chondrule AG164	7	−0.714	−0.340	0.032
Orgueil Meteorite (CI)				
Whole rock, AG94	8	0.003	0.002	0.000
Whole rock, AG95	8	−0.050	−0.015	0.011
Chainpur Meteorite (LL3)				
Matrix, AG76	4	0.059	0.050	0.019
Matrix, AG77	4	0.046	0.023	−0.001
Chondrule C11	4	−0.615	−0.307	0.013
Chondrule C12	4	−0.045	−0.027	−0.003
Evaporation products				
chondrule AH3, re-melted	7	6.718	3.444	−0.056
chondrule AG162, re-melted	7	0.861	0.459	0.010
chondrule AG163, re-melted	7	5.202	2.672	−0.038
chondrule AG164, re-melted	7	0.899	0.472	0.003

Sources: (1) Galy et al. 2001; (2) Chang et al. 2003; (3) Galy et al. 2002; (4) This study; (5) Young et al. 2002; (6) Galy et al. 2000; (7) Young et al. 2002; (8) Galy et al. in press

The definition of $\Delta^{25}Mg'$

In order to facilitate the analysis of fractionation laws it is convenient to amplify small differences in β using the $\Delta^{25}Mg$ notation. We define $\Delta^{25}Mg$ in a fashion analogous to $\Delta^{17}O$ as

$$\Delta^{25}Mg' = \delta^{25}Mg' - 0.521\,\delta^{26}Mg' \quad (18)$$

where 0.521 refers to the equilibrium value for β. It is important to recognize that we have defined the "big delta 25" in terms of the linear forms of the δ values, δ′ (data as represented in Table 2). We do this so that the β value used in the definition applies for all values of $\delta^{26}Mg'$. Using the usual, non-linear definitions of δ values in Equation (18) would cause $\Delta^{25}Mg$ to vary with $\delta^{26}Mg$ due simply to the curvature of the fractionation relationships in $\delta^{25}Mg$ - $\delta^{26}Mg$ space. The reader is reminded that this $\Delta^{25}Mg$ is not at all related to the $\Delta^{25}Mg$ often reported in the cosmochemistry literature (see section on nomenclature), nor is it the Δ used in some of the terrestrial stable isotope literature where $\Delta \sim 10^3 \ln\alpha$, i.e. the difference in δ values between two materials at equilibrium.

The values of $\Delta^{25}Mg'$ for a given datum are different on the SRM 980 and DSM3 scales. The SRM 980_O standard has a $\Delta^{25}Mg'$ value of +0.0315‰ on the DSM3 scale (Galy et al. 2003). Two analyses of CI carbonaceous chondrite and the clinopyroxene from a terrestrial mantle nodule have $\Delta^{25}Mg'$ values that are indistinguishable from 0.00 on the DSM3 scale (Table 2).

Uncertainties in $\Delta^{25}Mg'$

Uncertainties in $\Delta^{25}Mg'$ depend on the degree of covariance between $\delta^{25}Mg'$ and $\delta^{26}Mg'$ for each individual datum (i.e., the covariance for the internal precision defined by the variability among the measurement cycles on the mass spectrometer). Typical correlation coefficients between measured $\delta^{25}Mg'$ and $\delta^{26}Mg'$ on the MC-ICPMS instruments used by the authors are on the order of 0.8 (Young et al. 2002b), but variable. The corresponding covariance depends on the variances associated with the internal reproducibility of the measured $\delta^{25}Mg'$ and $\delta^{26}Mg'$ values. The reproducibility of individual measurements of $\delta^{25}Mg'$ and $\delta^{26}Mg'$ for solutions obtained in a single mass spectrometry session is on the order of ±0.015‰ and ±0.03‰ 1σ , yielding for the variances $\sigma^2_{\delta^{25}} = 0.00023$ and $\sigma^2_{\delta^{26}} = 0.0009$. These variances and the typical correlation coefficient in turn define a typical covariance $\sigma^2_{\delta^{25},\delta^{26}}$ for $\delta^{25}Mg'$ and $\delta^{26}Mg'$ of 0.00036. Standard propagation of errors leads to the following expression for the standard deviation for an individual $\Delta^{25}Mg'$ measurement:

$$\sigma^2_{\Delta^{25}Mg} = \sigma^2_{\delta^{25}Mg} + (-0.521)^2\,\sigma^2_{\delta^{26}Mg} + 2(-0.521)\,\sigma^2_{\delta^{25}Mg,\delta^{26}Mg} \quad (19)$$

Substitution of the typical variances and covariance into Equation (19) suggests that the $1\sigma_{\Delta^{25}Mg}$ for the MC-ICPMS measurements of Mg in solutions is on the order of ±0.010‰. This is regarded as an internal precision for an individual solution measurement. We note, however, that the reported measurements represent averages of several replicate analyses of the same solution and so more realistic assessments of the *internal precision* for $\Delta^{25}Mg'$ data presented here would be obtained from the uncertainties in the means (standard errors). For example, four analyses of the *same solution* yields a standard error for $\Delta^{25}Mg'$ of ±0.005‰ (this is still regarded as an internal precision because the effects of column chemistry and sample dissolution are not included). No attempt has been made here to review all of the raw data sets to calculate standard errors for each datum in Table 1. However, the distribution of data indicates that ±0.010‰ 1σ is an overestimate of the internal precision of $\Delta^{25}Mg'$ values and that a more realistic uncertainty is closer to a typical standard error, which in most cases will be ≤ ±0.005‰ (since the number of replicates is usually ≥4, e.g., Galy et al. 2001).

Δ′ – δ′ Diagrams

The role that different fractionation laws, and departures from them, play in determining Mg isotopic compositions is evident when the data are shown on a plot of $\Delta^{25}Mg'$ (ordinate) against $\delta^{26}Mg'$ or $\delta^{25}Mg'$ (abscissa). These Δ′-δ′ plots magnify differences that are difficult or impossible to see on the more traditional three isotope plots in which $\delta^{25}Mg$ is plotted against $\delta^{26}Mg$. Figure 3 shows how to interpret the Δ′-δ′ diagrams in terms of mass-dependent fractionation. The dashed and dash-dot lines mark the kinetic and equilibrium mass fractionation paths on such a diagram. The shaded areas bounded by these lines correspond to the regions of the diagram accessible from the origin by a single stage of mass fractionation. This single stage can have any slope between the two extremes shown (in fact, in some circumstances involving large molecules kinetic slopes could be steeper than that shown in Fig. 3). The dark grey arrows show two examples of the effects of two episodes of mass fractionation. In these examples, a kinetic fractionation process is followed by an equilibrium process. The regions outside the shaded areas are accessible only by multiple fractionation steps involving different fractionation laws.

Figure 4 shows how the additions or subtractions of radiogenic $^{26}Mg^*$ are manifested on the Δ′-δ′ plot. It is relevant for interpreting the meteorite Mg isotope data. The grey arrows show addition or subtraction of $^{26}Mg^*$ in the absence of mass fractionation relative to the origin (e.g., *in situ* growth of $^{26}Mg^*$ by decay of ^{26}Al). Starting with an initial composition at the origin, combinations of mass fractionation and variations in $^{26}Mg^*$ will define slopes

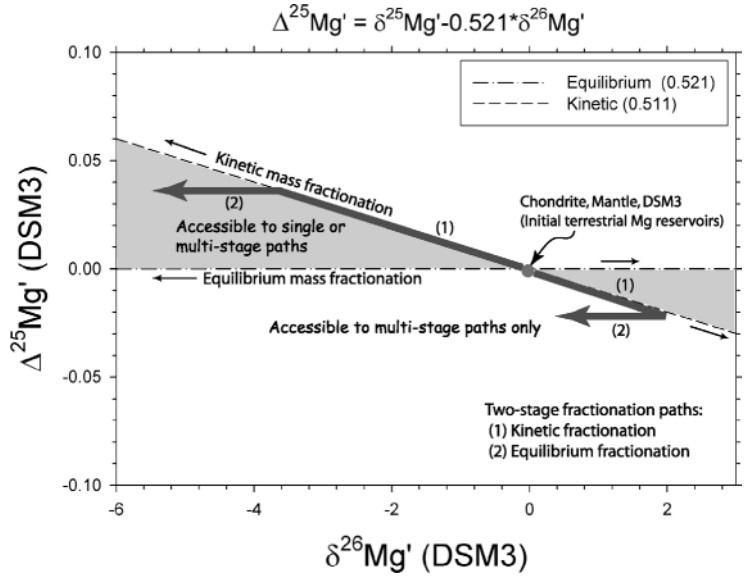

Figure 3. Schematic diagram illustrating how singe-stage and multiple-stage episodes of mass-dependent fractionation are expressed on a plot of $\Delta^{25}Mg'$ vs. $\delta^{26}Mg'$. The paths for pure equilibrium and pure kinetic fractionation relative to the origin are shown by the dashed-dot and dashed lines, respectively. The shaded region bounded by the kinetic and equilibrium fractionation lines is accessible from the origin by single stage fractionation. Other regions on the diagram are accessible by mass-dependent fractionation only if different fractionation laws are applied in succession (i.e., multiple steps with different β values). A variety of paths across the diagram are possible depending upon the nature and sign of the fractionation steps involved. Two multiple-stage paths are shown for illustration. In both examples a kinetic fractionation is followed by an equilibrium fractionation.

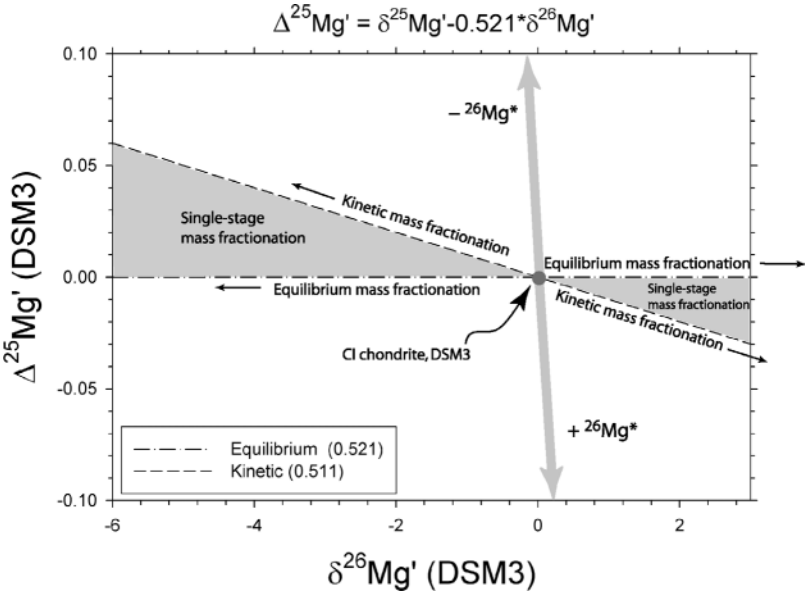

Figure 4. Schematic diagram illustrating how variations in the amount of radiogenic ^{26}Mg ($^{26}Mg^*$) are expressed on a plot of $\Delta^{25}Mg'$ vs. $\delta^{26}Mg'$. Pure addition of $^{26}Mg^*$ to a composition represented by the origin (e.g., CI chondrite) is manifest as a progression along the grey arrow pointing downward on the diagram. Single-step mass fractionation from the origin leads to compositions in the shaded regions bounded by the kinetic and equilibrium mass fractionation lines.

intermediate between the grey arrows and the shaded field bounded by the kinetic and equilibrium mass fractionation lines. On a plot of $\Delta^{25}Mg'$ against $\delta^{25}Mg'$ (rather than $\delta^{26}Mg'$, not shown in Fig. 4) addition and subtraction of $^{26}Mg^*$ results in a vertical path.

TERRESTRIAL MAGNESIUM ISOTOPE RESERVOIRS IN THREE-ISOTOPE SPACE: IMPLICATIONS FOR MECHANISMS OF FRACTIONATION

Measurements of terrestrial Mg isotope ratios on a plot of $\Delta^{25}Mg'$ vs. $\delta^{26}Mg'$ are all within the region bounded by the equilibrium and kinetic mass fractionation laws given expected uncertainties (Fig. 5). Apparently, all of the terrestrial reservoirs represented by the data thus far are related to the primitive chondrite/mantle reservoir by relatively simple fractionation histories. Adherence of the data to the regions accessible by simple mass fractionation processes in Figure 5 (the shaded regions in Fig. 3) is testimony to the veracity of the fractionation laws since there is no reason to suspect that Mg could be affected by any processes other than purely mass-dependent fractionation on Earth.

Casual inspection of Figure 5 suggests that Mg in waters is related to Mg from the primitive mantle (and chondrite) and evolved silicate crust (loess, continental basalt) by kinetic fractionation processes; most water data lie along the kinetic fractionation line that passes through mantle clinopyroxene with $\Delta^{25}Mg'$ values greater than crust and mantle. The same is true for spinach chlorophyll. Carbonates tend to be related to waters by a significant equilibrium fractionation component since their greatest variance is along a trend parallel to the equilibrium fractionation line at constant $\Delta^{25}Mg'$ (horizontal in Fig. 3). The fact that the carbonates tend to have positive $\Delta^{25}Mg'$ values relative to mantle/chondrite and silicate

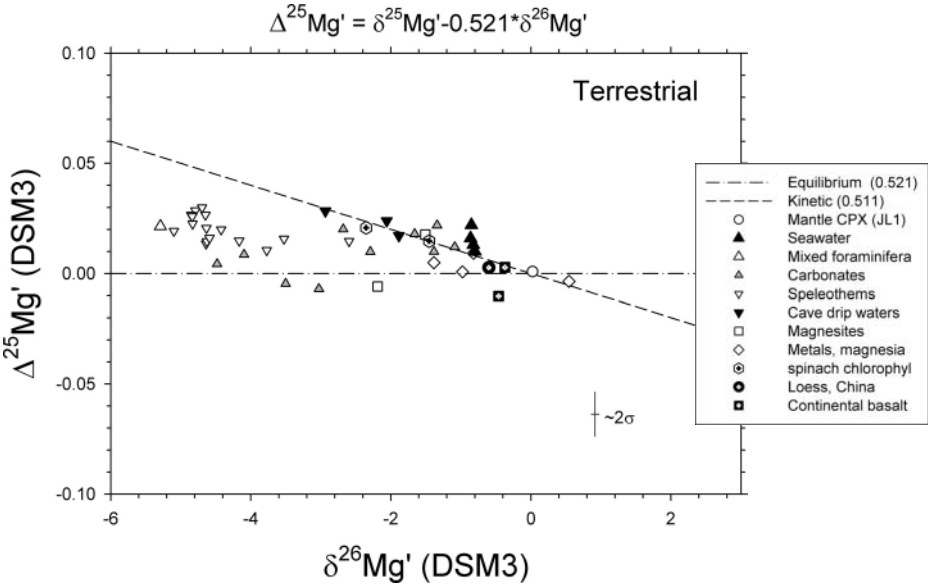

Figure 5. A plot of $\Delta^{25}Mg'$ vs. $\delta^{26}Mg'$ for terrestrial Mg materials. Within best estimates of uncertainties (cross) all of the data lie in the region bounded by equilibrium and kinetic mass fractionation laws. Waters, carbonates, and organic Mg (chlorophyll) have higher $\Delta^{25}Mg'$ values than mantle and crustal Mg reservoirs represented by mantle pyroxene, loess, and continental basalts. The difference in $\Delta^{25}Mg'$ values is attributable to episodes of kinetic mass fractionation.

crust can be explained by nearly equilibrium precipitation from waters that are themselves kinetically fractionated relative to mantle. These general observations can be quantified by extracting values for β from groups of genetically-related data.

For this purpose we applied the linear regression algorithms of Mahon (1996) to $\delta^{25}Mg'$ and $\delta^{26}Mg'$ values (Table 2) for subgroups of the data in Figure 5 to derive β values (β values are the slopes in $\delta^{25}Mg'$ -$\delta^{26}Mg'$ space). The results are listed in Table 3. The veracity of the technique was demonstrated recently by comparing the bulk Mg isotopic compositions of chondrules from the Allende and Bjurbole meteorites with residues left behind after the chondrules were partially evaporated in the laboratory (Young et al. 2002b). Evaporation of silicate liquids is a kinetic process that releases atomic Mg to the gas phase. The Mg isotopic compositions of the evaporation residues follow the predicted kinetic fractionation law for atomic Mg (Fig. 6), yielding a β value of 0.512 ± 0.002 (2σ) compared with the predicted

Table 3. Linear regression of $\delta^{25}Mg'$ and $\delta^{26}Mg'$ for groups of data from Table 1. Best-fit slopes are estimates of β for each data set.

Samples	Slope (β)	Low (95%)	High (95%)	Intercept ± 1σ	MSWD
Chlorophyll + Mg metal	0.512	0.510	0.514	0.031 ±0.002	1.49
Chondrule evaporation products	0.512	0.509	0.514	0.039 ±0.010	0.71
Mizpe Shlagim cave calcite + waters	0.522	0.517	0.527	0.013 ± 0.003	0.56
Soreq cave calcite + waters	0.519	0.517	0.520	0.020 ± 0.001	5.17
Dolostones + limestones + marble	0.524	0.518	0.531	0.004 ± 0.005	0.24

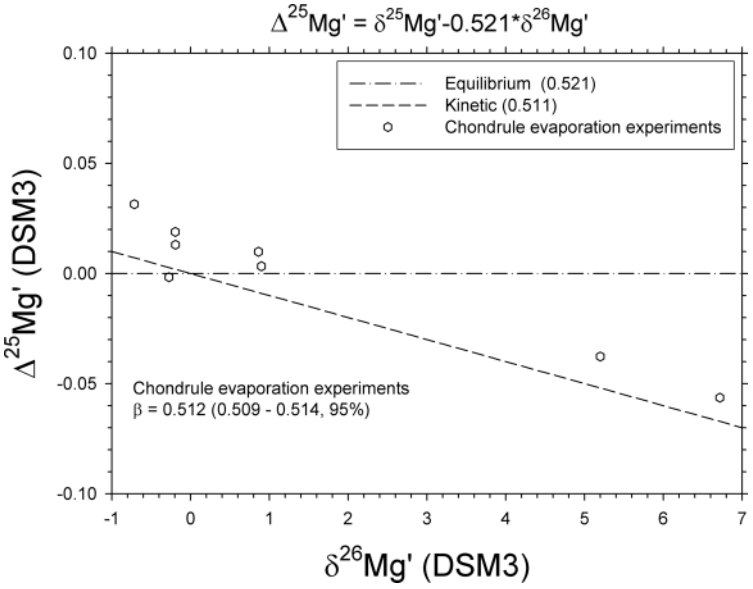

Figure 6. Plot of experimental products from evaporation of chondrules in the laboratory (Young et al. 2002b). The four data points below $\delta^{26}Mg' = 0.0$ are the starting materials. The evaporative residues exhibit heavy isotope enrichment along a kinetic mass fractionation path, verifying the prediction that evaporation should follow the kinetic mass fractionation law. The positive offset in $\Delta^{25}Mg'$ relative to DSM3 is a characteristic of the meteorite starting materials.

value of 0.511. The 95% confidence range in β for the evaporation experiments is 0.509–0.514 (Table 3) with an MSWD of 0.7, meaning that this kinetic β can be resolved with confidence from an equilibrium β value of 0.521. The intercept of the best-fit is 0.039‰, reflecting the positive $\Delta^{25}Mg'$ of the starting materials.

Extraction of β values from speleothems and waters apparently confirms the suspicion that Mg isotope partitioning during inorganic carbonate precipitation from waters is dominantly an equilibrium process (Fig. 7, Table 3). Linear regression of the $\delta^{25}Mg'$ and $\delta^{26}Mg'$ values for speleothem carbonates and associated drip waters and ground water from the Soreq cave site, Israel (Galy et al. 2002) yields a β of 0.519 ± 0.0015 (2σ) with the range being 0.517–0.520 at the 95% confidence level. Carbonate and drip water data for the Mitzpe Shlagim cave site, Israel, reported by Galy et al. (not shown in Fig. 7) yields a β of 0.522 ± 0.004 (2σ) and a 95% confidence range of 0.517–0.527. These values are near or indistinguishable from the equilibrium β of 0.521 and statistically far removed from the pure kinetic value of 0.511. Caution is warranted in the interpretation of these results because an equilibrium β does not exclude the possibility of a Rayleigh-like multi-step fractionation history in which the fractionation at each step is an equilibrium partitioning of the isotopes. The simplest interpretation, however, is that waters and their inorganic carbonate precipitates approach Mg isotopic equilibrium.

The β value defined by limestones, dolostones, marbles and seawater is consistent with equilibrium fractionation between aqueous Mg and carbonate Mg (Fig. 8, Table 3). The best-fit β is 0.524 ± 0.006 (2σ) with the 95% confidence range of 0.517–0.531. The data included in the regression represent an eclectic group of rocks, including three samples of marble (with the lowest $\Delta^{25}Mg'$ values near chondritic). However, there is some support for the equilibrium

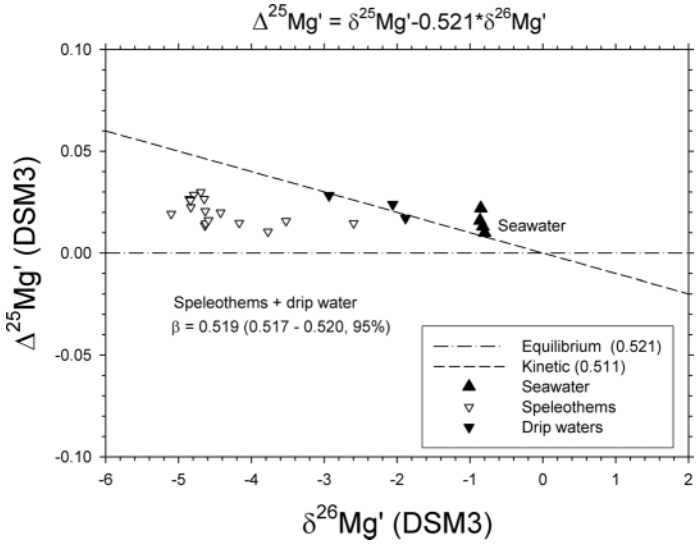

Figure 7. $\Delta^{25}Mg'$ vs. $\delta^{26}Mg'$ plot of calcite speleothems and their drip waters from the Soreq cave site, Israel (data from Galy et al. 2002) compared with seawater. The horizontal trend of the data suggests that Mg in carbonates is related to aqueous Mg by equilibrium fractionation processes. Results of a three-isotope regression, shown on the figure and in Table 3, confirm that the β value defined by the data is similar to the predicted equilibrium value of 0.521 and distinct from kinetic values. The positive $\Delta^{25}Mg'$ characteristic of the speleothem carbonates is apparently inherited from the waters. The positive $\Delta^{25}Mg'$ values of the waters appear to be produced by kinetic fractionation relative to primitive terrestrial Mg reservoirs (the origin).

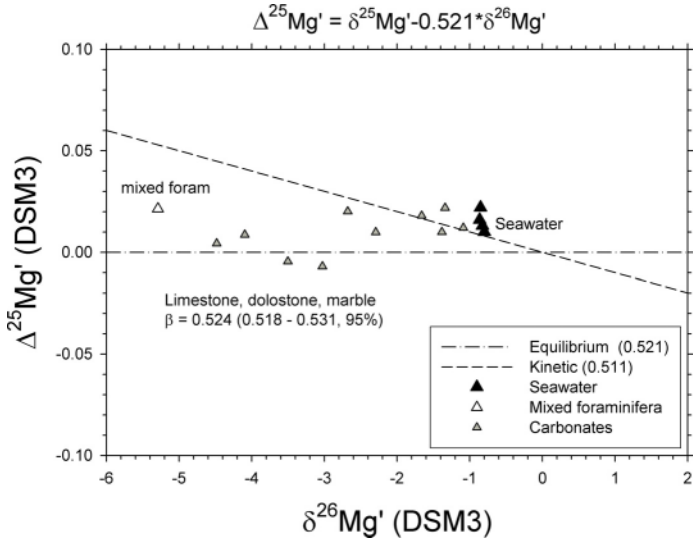

Figure 8. $\Delta^{25}Mg'$ vs. $\delta^{26}Mg'$ plot of limestone, dolostone, and marble samples (data from Galy et al. 2002) compared with a sample of foraminifera of various species (Chang et al. 2003) and seawater (Chang et al. 2003, this study). The broadly horizontal trend of the carbonates at elevated $\Delta^{25}Mg'$ suggests a component of equilibrium fractionation relative to seawater. The β value derived by regression of these $\delta^{25}Mg'$ and $\delta^{26}Mg'$ data is within the range for equilibrium fractionation and statistically distinguishable from purely kinetic fractionation.

relationship between marine carbonates and seawater from the mixed-species foraminifera analysis reported by Chang et al. (2003). Figure 8 shows that the mixed foraminifera and seawater have similar positive $\Delta^{25}Mg'$ values, meaning that the fractionation relationship between them is essentially equilibrium. However, it is also true that the foraminifera-seawater fractionation is the largest terrestrial difference observed to date and so vital effects might be expected. More work is required!

The analysis of fractionation law exponents quantifies the impression from the Δ'-δ' plots that aqueous Mg is related to primitive mantle and average crustal Mg by kinetic processes while carbonates precipitated from waters approach isotopic equilibrium with aqueous Mg. In any case, the positive $\Delta^{25}Mg'$ values of carbonates relative to the primitive chondrite/mantle reservoir and crust is a robust feature of the data and requires a component of kinetic Mg isotope fractionation prior to carbonate formation, as illustrated schematically in Figure 3.

Magnesium metal and chlorophyll Mg isotope ratios (lumped together because both are expected to exhibit kinetic effects) reported by Galy et al. (2001) define a best-fit β value of 0.512 ± 0.002 (2σ) and a 95% confidence range of 0.510 to 0.514 (Fig. 9, Table 3). This β is indistinguishable from the nominal kinetic value of 0.511 and statistically distinct from the equilibrium value of 0.521, and it is evidence for kinetic fractionation of the Mg isotopes among these materials, as one might expect from them. Again, more work is required, but these first results show that there is potential for distinguishing equilibrium from kinetic Mg exchange in natural systems using isotopes.

EXTRATERRESTRIAL MAGNESIUM ISOTOPE RESERVOIRS IN THREE-ISOTOPE SPACE

The meteorite data (Fig. 10) are not related by simple mass fractionation. They exhibit a clear negative trend in $\Delta^{25}Mg'$ -$\delta^{26}Mg'$ space that can be explained by a combination of the presence of excess $^{26}Mg^*$ due to decay of short-lived and extinct ^{26}Al and a mass-fractionation component (cf., Fig. 4). This is most easily seen on a plot of $\Delta^{25}Mg'$ vs. $\delta^{25}Mg'$ where decay of ^{26}Al in the absence of fractionation would result in a vertical trend (Fig. 11). The trend is dominated by the Allende chondrules with negative $\Delta^{25}Mg'$ in the data set but there are hints (e.g., the Bjurbole chondrules) that the trend may extend to positive $\Delta^{25}Mg'$ as well. A positive $\Delta^{25}Mg'$ may signify that bulk Earth has more radiogenic ^{26}Mg than these primitive samples. Alternatively, it may mean that there are small anomalies in the Mg isotopic system (e.g., excesses in ^{24}Mg) at the 0.03‰ level.

The simplest interpretation of the linear trend in Figure 10 (and 11) is that it is a mixing relationship. One endmember of the mixing trend is surely CAI material for which there is overwhelming evidence for *in situ* decay of ^{26}Al from an Al reservoir with an initial $^{26}Al/^{27}Al$ of about 5×10^{-5} (MacPherson et al. 1995), although the precise value for the initial $^{26}Al/^{27}Al$ recorded by CAIs is debated (see the section on laser ablation). The evidence for *in situ* decay in the other materials is not so clear. For all of the objects in the plot there must be just the right combination of *in situ* ^{26}Al decay and mass fractionation such that the combination of the two phenomena results in a strong correlation between $^{26}Mg^*$ and mass fractionation. Mixing appears to be the only plausible process capable of achieving this end unless one resorts to highly strained hypotheses. The single existing high-precision analysis of a bulk CAI (from Allende) published at the time of this writing has high $\delta^{26}Mg'$ and low $\Delta^{25}Mg'$ due to the presence of highly fractionated Mg and $^{26}Mg^*$ (Galy et al. 2000). The trend of the other chondrite data is in general from the origin towards the CAI datum (Fig. 12). Mixing between the highly fractionated CAI materials containing $^{26}Mg^*$ and more magnesian materials with no $^{26}Mg^*$ could produce the negative correlation between $\Delta^{25}Mg'$ and $\delta^{26}Mg'$. Mixing in this plot should produce a straight line. In detail the extension of the linear trend misses the one

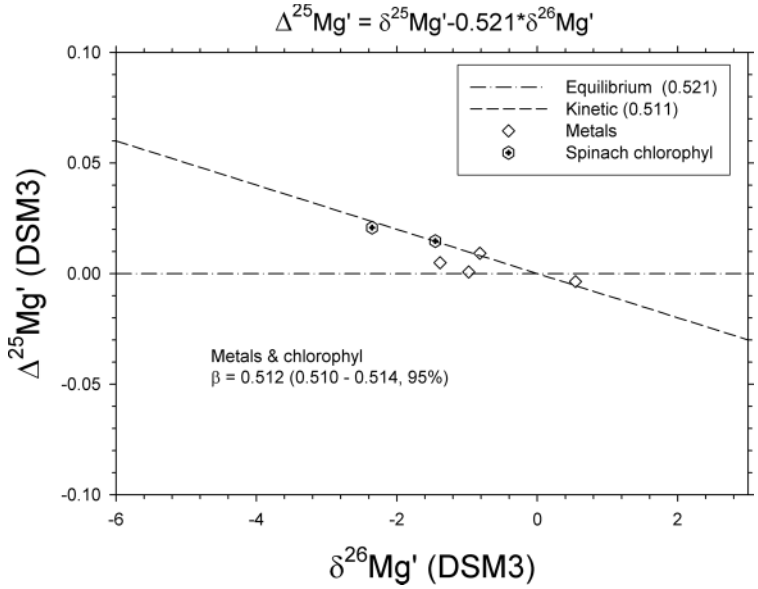

Figure 9. $\Delta^{25}Mg'$ vs. $\delta^{26}Mg'$ plot showing that Mg metals and Mg from chlorophyll, both representing Mg that is likely to be fractionated by kinetic processes relative to primitive terrestrial Mg reservoirs (the origin), follow a kinetic fractionation path relative to the origin. The β value derived by regression of these $\delta^{25}Mg'$ and $\delta^{26}Mg'$ data is statistically indistinguishable from the kinetic value of 0.511 and clearly resolved from the equilibrium value of 0.521.

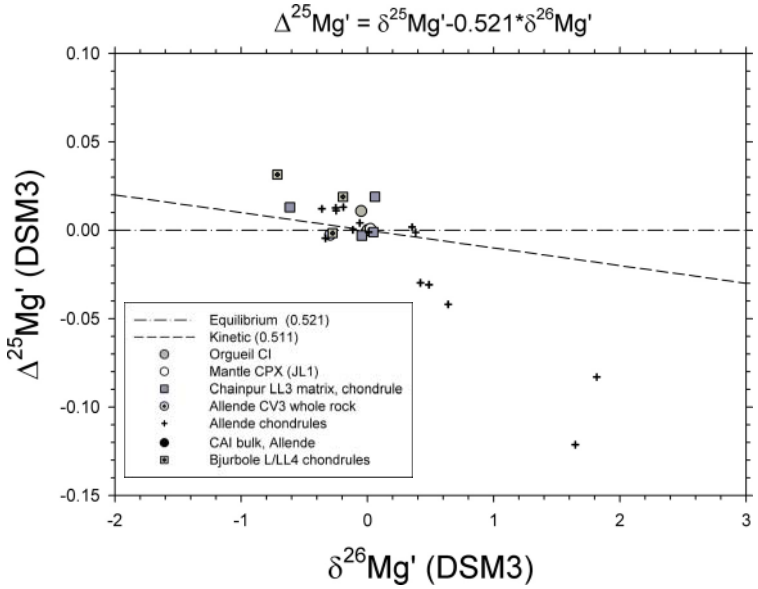

Figure 10. $\Delta^{25}Mg'$ vs. $\delta^{26}Mg'$ plot showing that the chondrite meteorite data define a trend inconsistent with mass-dependent fractionation. A single whole-rock CAI sample with the lowest $\Delta^{25}Mg'$ value plots off the diagram to the lower right.

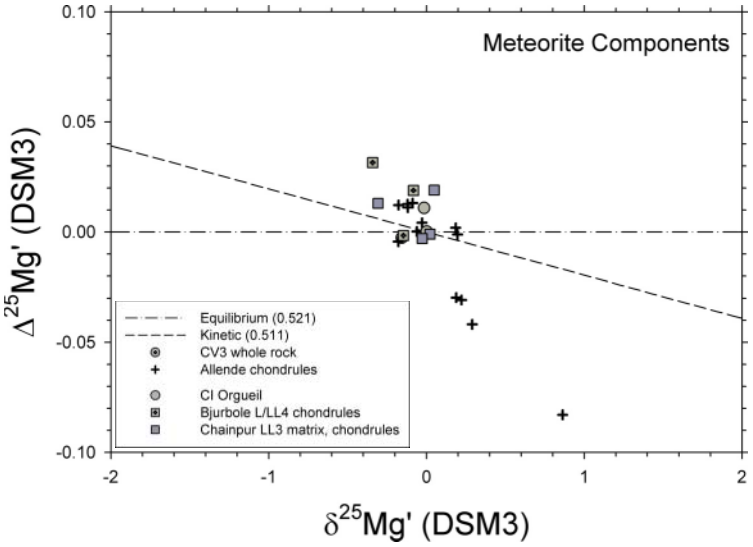

Figure 11. $\Delta^{25}Mg'$ vs. $\delta^{25}Mg'$ plot similar to Figure 10. In this diagram addition of $\delta^{26}Mg^*$ by ^{26}Al β+ decay results in a vertical trend. The trend of the data shows that they can only be explained by a *combination* of mass-dependent fractionation and addition of $^{26}Mg^*$. The regularity of the trend among different chondritic components argues for a mixing line.

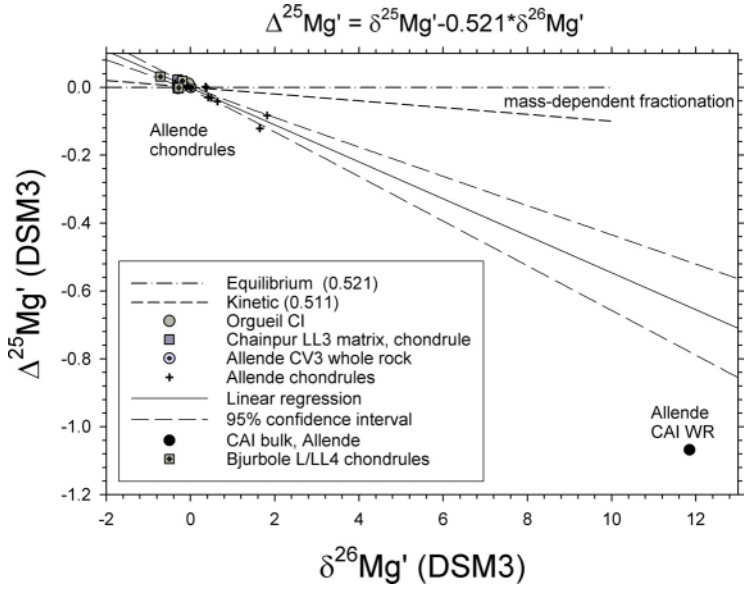

Figure 12. Linear regression of chondrite data in $\Delta^{25}Mg'$ vs. $\delta^{26}Mg$ space compared with the whole-rock composition of an Allende CAI.

existing CAI datum. However, although we have only one whole-rock CAI sample analyzed by MC-ICPMS there are enough existing TIMS, secondary ion mass spectrometry (SIMS), and laser ablation MC-ICPMS data (published and unpublished) to safely say that CAIs do not have a unique bulk Mg isotopic composition (Clayton et al. 1988; Clayton and Mayeda 1977; Goswami et al. 1994; Kennedy et al. 1997; Russell et al. 1998; Wasserburg et al. 1977; Young et al. 2002a). In order to evaluate the likelihood that all of the variability in $\Delta^{25}Mg'$ seen in Figures 10–12 is due to mixing with CAIs, many more CAI whole rock analyses will be required.

If mixing between CAIs is the cause of the variable $\Delta^{25}Mg'$ among the Allende chondrules and other chondrite constituents shown here, then the departures of the chondrule and matrix data from mass fractionation is not indicative of *in situ* growth of extinct ^{26}Al in these objects but is instead due to inheritance of the product $^{26}Mg^*$ from ^{26}Al decay in the CAIs. The extent to which these high-precision Mg isotope data can be interpreted in terms of mixing rather than *in situ* decay of ^{26}Al was discussed by Galy et al. (2000). Indeed the origin of $^{26}Mg^*$ in Al-rich chondrules has been debated for years. The question is the extent to which the presence of $^{26}Mg^*$ in these non-CAI objects can be used to infer information about the timing of their formation. The problem is exacerbated by the fact that the mixing between Mg-rich chondritic materials and the Al-rich, Mg-poor and $^{26}Mg^*$-rich CAIs could result in correlations between $^{26}Mg^*$ and Al/Mg (Fig. 13). Such correlations are regarded as tell-tale signs of in situ decay of ^{26}Al; mixing lines resemble isochrons on ^{25}Mg-^{26}Al evolution diagrams and yet have no chronological meaning for the early Solar System.

A test of the hypothesis that the linear trends in Figures 10–12 are due to mixing comes from comparisons with oxygen isotopes. It has been conventional wisdom that $^{26}Mg^*$ does not correlate in detail with ^{16}O excesses in primitive chondrite components, including CAIs. However, combining the new highly precise MC-ICPMS data with isotope ratio data for the

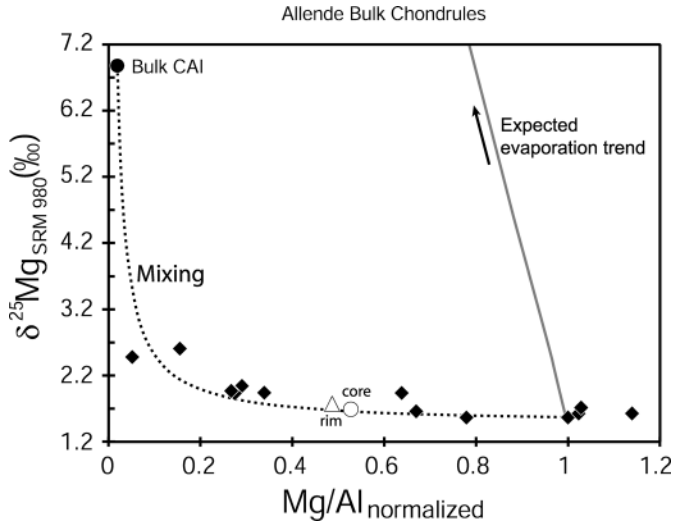

Figure 13. Whole-rock Allende chondrules plotted in $\delta^{25}Mg$ (SRM 980_O) vs. Mg/Al space showing that a mixing curve (dotted line) between the CAI whole-rock sample and the Mg-rich, Al-poor chondrules (i.e., "chondritic" chondrules) fits the trend defined by the bulk chondrule data (modified after Galy et al. 2000). The expected evaporation trend is shown for comparison and represents the consequences of free evaporation of chondrules in space. The evaporation curve is described in greater detail by Galy et al. (2000).

same materials suggests that such a correlation may exist. Figure 14 shows $\Delta^{25}Mg'$ data for components of various carbonaceous chondrite and ordinary chondrite meteorites, including Allende (CV3) matrix, Allende chondrules, Orgueil (CI) whole rocks, Chainpur (LL3) matrix/whole rock, and Bjurbole (L/LL4) chondrules collected by MC-ICPMS compared with $\Delta^{17}O$ (a measure of ^{16}O excess) obtained by laser ablation of the same materials in the author's laboratory or from the literature (Table 4). There is an overall correspondence between low $\Delta^{17}O$ (high concentrations of excess ^{16}O) and low $\Delta^{25}Mg'$ (high concentrations of excess ^{26}Mg) evident in these data. Addition of the CAI datum under the assumption that the CAI has a $\Delta^{17}O$ corresponding to the most enriched whole rocks (e.g., Clayton et al. 1977) (an assumption that may be justified if the $\Delta^{17}O$ of many CAIs was increased due to alteration either in the solar nebula or on the meteorite parent bodies) completes the trend (Fig. 15). The data resemble a hyperbolic curve in $\Delta^{25}Mg'$ - $\Delta^{17}O$ space. Hyperbolic mixing curves would result if the two endmember components had different Mg/O ratios.

The possibility for mixing between a CAI-like endmember characterized by a ^{16}O excess, a low Mg/O, and high $^{26}Mg^*$ (call it "CAI") with a "chondritic" endmember that is low in ^{16}O excess, higher in Mg/O, and has no $^{26}Mg^*$ is quantified by overlaying the data with hyperbolic mixing curves between these endmembers in Figure 15. The curvature of the mixing lines depends on $(Mg/O)_{(CAI)}/(Mg/O)_{(chondritic)}$. The calculation assumes a single composition for both endmembers, an oversimplification to be sure. Nonetheless, with this assumption the data are explained by $(Mg/O)_{(CAI)}/(Mg/O)_{(chondritic)}$ ranging from 0.2–0.02 (Fig. 15). These values are not unreasonable in view of the different chemical compositions of the Mg-rich "chondritic" objects like chondrules and matrix and the Mg-poor CAIs.

Many more high-precision whole-rock analyses of both Mg and O isotope ratios for chondrite components would help to establish whether or not the mixing trends in Figure 15 are valid, or even if the concept of mixing is useful. Bulk objects are desirable because their isotopic compositions are not affected by secondary inter-mineral exchange reactions that are know to be important for both the Mg and O isotopic systems in CAIs and chondrules.

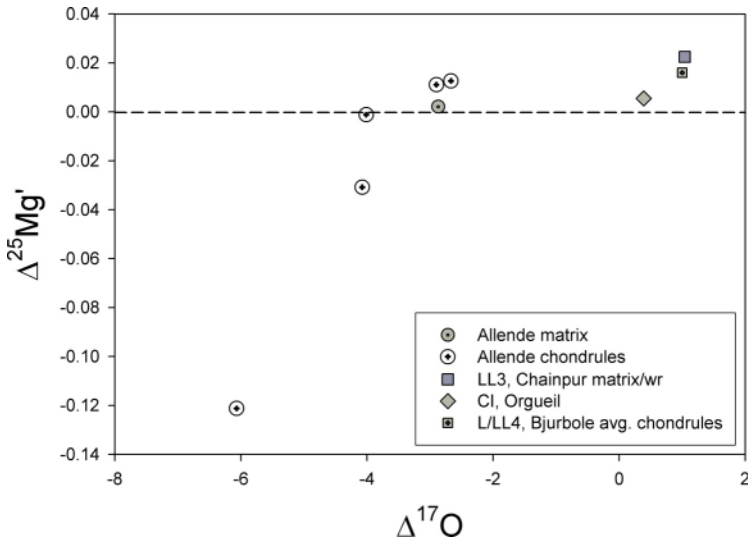

Figure 14. Comparison of $\Delta^{25}Mg'$ (DSM3) and $\Delta^{17}O$ (SMOW) values for various chondrules and whole-rock chondrite samples. The sources of the oxygen isotope data are given in Table 3. Aqueous alteration on this diagram will move points approximately horizontally on this diagram.

Table 4. Tabulation of $\Delta^{25}Mg'$ vs. $\Delta^{17}O$ for various chondrite components. $\Delta^{17}O$ laser ablation data are shown explicitly to demonstrate that averages are reflective of the bulk objects. Where data are few, the objects are small in comparison to laser beam diameter.

Sample	$\Delta^{25}Mg'$ [5]	$\Delta^{17}O$
Allende (CV3) matrix	0.002	−2.87 [1]
Allende chondrule A3	0.011	−2.48 −3.42 −2.58 −3.17 −3.02 −3.25 −3.23 −3.17 −2.31 −2.43 −2.92 −3.02 −2.65 −2.99 Avg = −2.90±0.35 1σ [2]
Allende chondrule A4	−0.121	−6.5 −5.7 −6 Avg = −6.07±0.40 1σ [2]
Allende chondrule A5	−0.031	−4.5 −4 −3.5 −4.3 Avg = −0.408±0.44 1σ [2]
Allende chondrule A6	−0.001	−3.8 −3.4 −4.5 −3.7 −4.3 −3.9 −3.9 −4.8 −3.8 Avg = −4.01±0.44 1σ [2]
Allende chondrule A7	0.013	−2.9 −2.7 −2.4 Avg = −2.67±0.25 1σ [2]
Allende CAI whole rock	−1.07	−19.2 [1]
Orgueil (CI)	0.006±0.001 1σ	0.39 [2]
Chainpur (LL3) matrix/wr	0.022	1.04 [4]
Bjurbole (L/LL4) avg. chondrules	0.016±0.017 1σ	1.00 [4]

[1] Data from Clayton and Mayeda 1999
[2] Data from Young et al. 2002a
[3] Value based on the assumption that the CAI has the maximum ^{16}O enrichment typical for Allende
[4] Data from Clayton et al. 1991
[5] Uncertainties on the order of 0.01 as discussed in text.

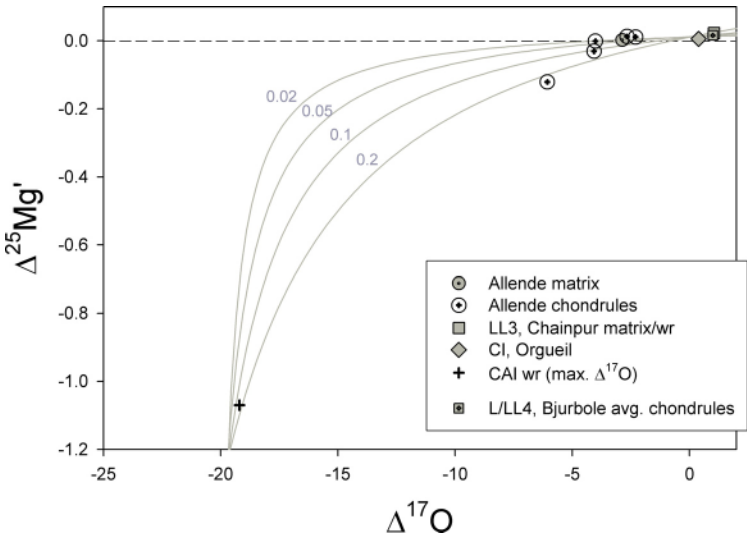

Figure 15. Hyperbolic mixing curves between a "typical" chondritic endmember at high $\Delta^{17}O$ (SMOW) and $\Delta^{25}Mg'$ (DSM3) and a "typical" CAI composition at low $\Delta^{17}O$ and $\Delta^{25}Mg'$ compared with existing high-precision data. The curvature of the mixing lines is a function of $(Mg/O)_{CAI}/(Mg/O)_{chondrite}$ where "CAI" and "chondrite" refers to the two endmember compositions. Each curve is labeled with the corresponding $(Mg/O)_{CAI}/(Mg/O)_{chondrite}$ values.

The whole-rock samples are not immune from other open-system exchange, however. For example, we do not yet know how aqueous alteration manifests itself on these diagrams because detailed studies of the Mg isotopic effects of water-rock reactions have not been carried out at the time of this writing.

ISOTOPIC COSMOBAROMETRY

The vast majority of the Mg isotope variability seen in the components of primitive meteorites and their constituents is apparently attributable to mixing with the highly mass fractionated and radiogenic Mg in CAIs (Fig. 10). Even if the mixing hypothesis proves to be incorrect, the amount of variability among chondrules is small in comparison to what one would expect. This is because the chondrules were once molten spheres in space and the expectation is that they should show evidence for evaporation. However, the high-precision Mg isotope data do not follow the trends expected if the molten spheres were present in a near vacuum. The lack of isotope fractionation in chondrules is not peculiar to Mg and is observed in K and Fe as well (Alexander et al. 2000; Galy et al. 2000; Alexander and Wang 2001; Zhu et al. 2001). It contrasts with the large fractionation effects seen in CAIs (Clayton et al. 1988). The general lack of light-element mass fractionation in chondrules has been a vexing problem because these objects show evidence for volatility-controlled variations in the concentrations of the very same elements lacking isotope fractionation, at odds with the expectations for free evaporation (Fig. 13) (Galy et al. 2000).

Two theories exist for the lack of isotope fractionation in chondrules. Both rely on the concept of quasi-statical (i.e., almost equilibrium) exchange of isotopes between liquid and gas followed by permanent loss of rock-forming elements to the escaping gas phase. One model (Alexander 2003) implies that the chondrules formed in such close proximity to one

another that the partial pressures of the rock-forming elements in the surrounding ambient gas approached saturation (Fig. 16). The other (Richter et al. 2002) does not rely upon widespread saturation of the gas. Instead it allows that the liquid chondrules exchanged isotopes with the gas evaporating from the object. The local atmosphere of gas is bound to its chondrule by slow diffusion through the ambient gas (Fig. 16). The differences between these two physical situations can be seen with reference to an equation describing the net flux of a component *i* (e.g., Mg) volatilizing from a molten sphere (Richter et al. 2002):

$$J_{i,\mathrm{net}} = \frac{J_{i,\mathrm{evap}}\left(1-\frac{P_{i,\infty}}{P_{i,\mathrm{sat}}}\right)}{1+\frac{\gamma_i r}{D_{i,\mathrm{gas}}}\sqrt{\frac{RT}{2\pi m_i}}} \tag{20}$$

or

$$J_{i,\mathrm{net}} = \frac{J_{i,\mathrm{evap}}\left(1-\frac{P_{i,\infty}}{P_{i,\mathrm{sat}}}\right)}{1+\Gamma} \tag{21}$$

where $J_{i,\mathrm{net}}$ is the net difference between the evaporative and condensation fluxes for species *i*, $J_{i,\mathrm{evap}}$ is the evaporative flux of *i*, $P_{i,\infty}$ is the partial pressure of species *i* far removed from the molten object, $P_{i,\mathrm{sat}}$ is the saturation partial pressure of *i*, $D_{i,\mathrm{gas}}$ is the diffusion coefficient of *i* through the gas phase, γ_i is the evaporation factor for *i*, *r* is the radius of the molten object, and m_i is the mass of the volatilizing species. In terms of this equation, isotope fractionation will occur when $J_{i,\mathrm{net}}/J_{i,\mathrm{evap}} \rightarrow 1$ while no fractionation occurs when $J_{i,\mathrm{net}}/J_{i,\mathrm{evap}} \rightarrow 0$. The latter occurs where the background pressure $P_{i,\infty}$ approaches the saturation pressure $P_{i,\mathrm{sat}}$. This could be

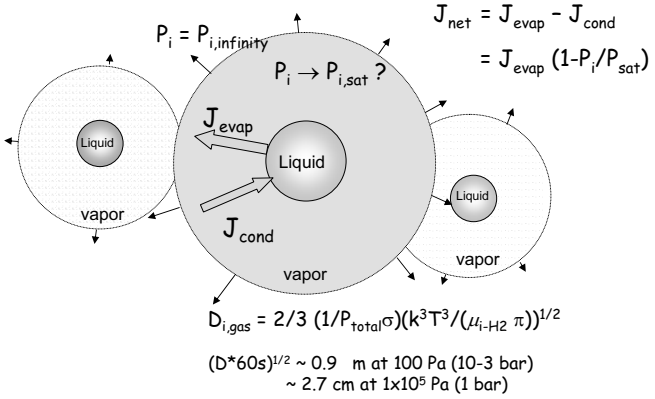

Figure 16. Schematic illustration of envelopes of gas species *i,* in this case Mg, surrounding a volatilizing molten chondrule in space. The size of the gas envelope is a function of ambient background pressure P_∞ by virtue of the effect that pressure has on the gas molecule diffusivity D_i. The diffusion coefficient can be calculated from the kinetic theory of gases, as shown. The level of isotopic fractionation associated with volatilization of the molten chondrule depends upon the balance between the evaporative flux J_{evap} and the condensation flux J_{cond}. When the fluxes are equal (i.e., when $J_{net} = 0$), there is no mass-dependent isotope fractionation associated with volatilization. This will be the case when the local partial pressure P_i approaches the saturation partial pressure $P_{i,sat}$

the case where a population of volatilizing chondrules contributes to an elevated background of partial pressure of rock-forming elements as envisioned by Alexander (2003). In the other extreme where $P_{i,\mathrm{sat}} >> P_{i,\infty}$, as would be the case where chondrules are not sufficiently close together to cause a pervasive rise in background partial pressures, the only way to prevent fractionation is for Γ to be large, as suggested by Galy et al. (2000). The kinetic theory of gases permits one to compute Γ as a function of pressure. Such calculations show that Γ is large enough to preclude fractionation when total pressures approach 1 bar (e.g., at T = 2000 K and $\gamma_i = 0.06$, $\Gamma = 0.062$ at 10^{-3} bar and 62 at 1 bar for a chondrule-sized object).

From the preceding discussion it should be clear that the level of isotopic fractionation for a major rock-forming element like Mg in an object that was once molten in the early Solar System is a barometer of either total pressure (large Γ) or partial pressures relative to saturation (small Γ). In order to use Mg as a "cosmobarometer," high-precision analyses of Mg isotope ratios in both chondrules and CAIs are required.

CAI's that were once molten (type B and compact type A) apparently crystallized under conditions where both partial pressures and total pressures were low because they exhibit marked fractionation of Mg isotopes relative to "chondritic" isotope ratios. But much remains to be learned from the distribution of this fractionation. Models and laboratory experiments indicate that Mg, O, and Si should fractionate to different degrees in a CAI (Davis et al. 1990; Richter et al. 2002) commensurate with the different equilibrium vapor pressures of Mg, SiO and other O-bearing species. Only now, with the advent of more precise mass spectrometry and sampling techniques, is it possible to search for these differences. Also, models predict that there should be variations in isotope ratios with growth direction and Mg/Al content in minerals like melilite. Identification of such trends would verify the validity of the theory. Conversely, if no correlations between position, mineral composition, and Mg, Si, and O isotopic composition are found in once molten CAIs, it implies that the objects acquired their isotopic signals prior to final crystallization. Evidence of this nature could be used to determine which objects were melted more than once.

From the high-precision Mg isotope data (and other K and Fe isotope data) available to date, it appears that chondrules crystallized under conditions of either high Γ, meaning high total pressure, or in close proximity to one another where $P_{i,\mathrm{sat}} \sim P_{i,\infty}$. There are some mass-dependent Mg isotopic heterogeneities in some chondrules when the objects are examined using laser ablation (see below) (Young et al. 2002a). We do not yet know how fractionation relates to mineralogy nor do we know if different populations of chondrules have different degrees of isotopic variability. More data are required before we can have confidence in the meaning of heterogeneity in Mg isotope fractionation in chondrules.

IN SITU LASER ABLATION

Young et al. (2002a) showed that ultraviolet laser ablation combined with MC-ICPMS (LA-MC-ICPMS) can offer advantages over other methods of spatially resolved Mg isotopic analysis of meteorite materials. They collected data for chondrules and a CAI from the Allende meteorite. Each datum in that study represents approximately 2.8 μg of material (based on a laser spot diameter of 100 μm and laser pit depth of 30 μm; depths are uncertain to ± 20%).

Allende chondrules exhibit internal mass-dependent variations in δ^{25}Mg values that deviate from the "canonical" chondritic value (we focus on ^{25}Mg/^{24}Mg here to avoid the ambiguities surrounding ^{26}Mg*) (Young et al. 2002a). One reason for this variation might be secondary alteration that appears to be associated with low ^{25}Mg/^{24}Mg relative to the matrix of the meteorite. The other is that portions of chondrules containing abundant relic grains of refractory olivine have high ^{25}Mg/^{24}Mg relative to matrix.

Alteration in Allende chondrule C6 is concentrated at the margins where δ^{25}Mg values are low (Fig. 17). Evaluation of the likelihood that low δ^{25}Mg values could be the result of aqueous alteration will require studies of Mg isotope fractionation during low-T alteration of terrestrial mafic rocks. An alternative explanation is that low δ^{25}Mg and alteration resulted from condensation (collision frequency of gaseous Mg is greater for the lighter isotopes).

Laser spots from unaltered parts of a CAI (USNM 3576-1) from Allende have the same ^{25}Mg/^{24}Mg ratio within analytical uncertainties with a mean δ^{25}Mg value of 5.3‰ ± 0.1 (2σ) on the SRM 980_O scale (Fig. 18), corresponding to +3.54‰ on the DSM3 scale. The laser ablation spot that sampled alteration at fassaite (Ti-Al-rich diopside)-anorthite grain boundaries yields a higher δ^{25}Mg of 5.6‰ (3.84‰ DSM3) (Fig. 18). These same laser spot samples vary in δ^{26}Mg by 1‰ (Fig. 18) as the result of in-growth of ^{26}Mg by decay of ^{26}Al.

Uniformity in δ^{25}Mg among unaltered phases in CAI USNM 3576-1 is noteworthy because these high-precision analyses were obtained without normalization to a single ^{25}Mg/^{24}Mg value. Previous measurements of δ^{26}Mg* (δ^{26}Mg* is the excess in δ^{26}Mg relative to mass fractionation shown by the dashed line in Fig. 18) in CAIs were all made either by TIMS or SIMS. A uniform δ^{25}Mg is imposed on the TIMS data because the high-precision δ^{26}Mg* values are obtained by normalizing to a single "terrestrial" ^{25}Mg/^{24}Mg. The detection limit for δ^{26}Mg* by SIMS is sufficiently high that δ^{26}Mg* can only be detected with certainty in the most aluminous phases, including gehlenitic melilite (Al/Mg > 10), hibonite (Al/Mg > 15), and feldspar (Al/Mg > 200) (Sahijpal et al. 1998). New innovations in SIMS techniques (e.g., multi-collection) show promise for lowering detection limits, but at present the laser ablation MC-ICPMS data are unique in that they show unequivocal δ^{26}Mg* in the low Al/Mg minerals, including fassaite (Ti-Al-rich diopside) and spinel. A spread in δ^{26}Mg values at constant δ^{25}Mg among the low-Al minerals sampled by the laser, together with correlation between δ^{26}Mg* and ^{27}Al/^{24}Mg (Fig. 19), is clear indication that ^{26}Mg was added independently of ^{25}Mg by decay of ^{26}Al in these minerals. Analyses with the greatest Al and highest δ^{26}Mg* values in this study come from the gehlenitic melilite typical of the margin of the CAI.

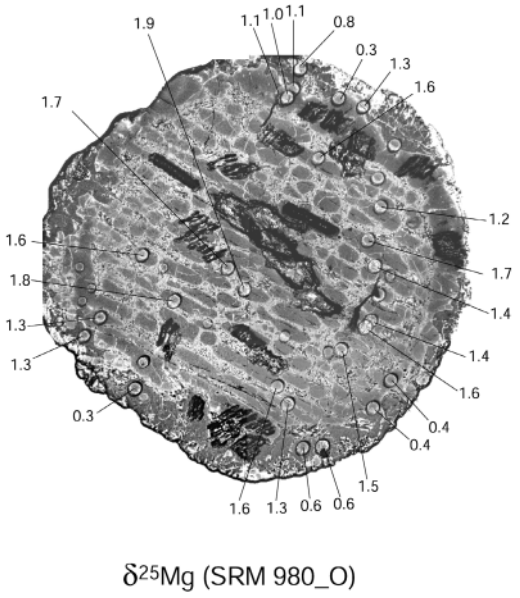

Figure 17. A backscattered electron image of a barred olivine chondrule from the Allende meteorite (chondrule C6l, after Young et al. 2002a) showing the locations of ultraviolet laser ablation pits (each pit is 100 μm in diameter) and the δ^{25}Mg values (SRM 980_O) obtained from the pits by LA-MC-ICPMS. Darkest areas around the margins are pyroxenes. Olivine bars appear as medium gray tones. The brighter mottled areas are altered mesostasis interstitial to the olivine bars. Large dark trenches are vestiges of oxygen isotope laser ablation pits.

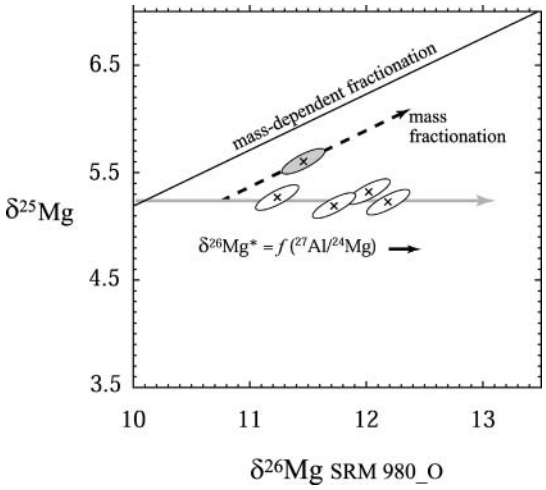

Figure 18. Magnesium three-isotope plot (relative to SRM 980_O) showing laser ablation data for Allende CAI 3576-1 (after Young et al. 2002a). Ellipses represent the 95% confidence for each datum. The shaded datum is the analysis that included alteration material in the CAI. This point is related to the others by mass fractionation (dashed line) at constant $\delta^{26}Mg^*$ where $\delta^{26}Mg^*$ is the horizontal deviation from a terrestrial mass-fractionation curve. The $\delta^{26}Mg^*$ value depends on the Al/Mg ratio, indicating *in situ* decay of ^{26}Al in the CAI. The high precision of the MC-ICPMS analyses makes it possible to resolve mass-dependent fractionation from excesses in ^{26}Mg at the sub-per mil level.

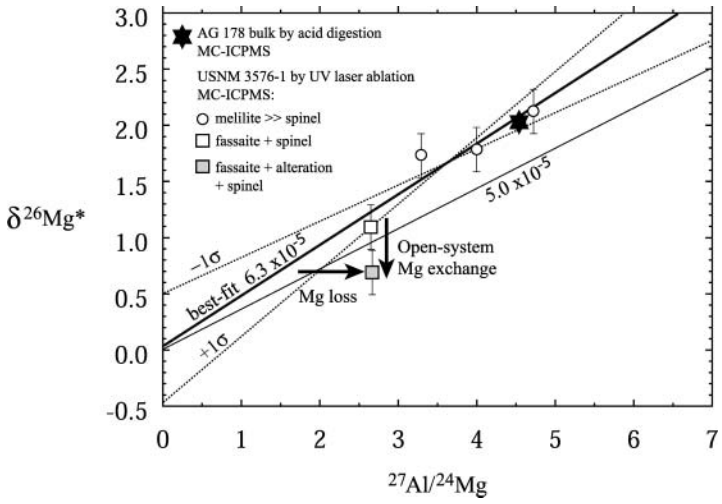

Figure 19. $^{26}Mg^*$-Al evolution diagram for for Allende CAI USNM 3576-1 obtained by LA-MC-ICPMS. Linear regression of the data in which alteration is absent (open symbols) yields an estimate of the initial $^{26}Al/^{27}Al$ for the sample (6.3×10^{-5}) based on the equation $\delta^{26}Mg^* = (^{26}Al/^{27}Al)_{initial}\ (10^3/(^{26}Mg/^{24}Mg)_{SRM\ 980})\ (^{27}Al/^{24}Mg)$ and the $(^{26}Mg/^{24}Mg)_{SRM\ 980}$ value of Catanzaro et al. (1966). This estimate is indistinguishable from the value suggested by comparing the origin with a whole-rock sample of an Allende CAI measured by MC-ICPMS and reported by Galy et al. (2000). The uncertainties in the whole rock value are smaller than the star symbol. The position of the datum that includes alteration (grey symbol) requires either open-system exchange of Mg with an external reservoir or open-system loss of Mg from the alteration zone by leaching.

The distinct $\delta^{25}Mg$ value for the altered portion of the CAI suggests that alteration occurred in an open system. The data could be explained by closed-system Mg exchange if there was a reservoir within the CAI that had lower $^{26}Mg^*$ than the altered spot. However, there is no such reservoir; the altered material has the lowest Al/Mg present in the object. Open system deviations from a correlation line in Figure 19 are expected because Mg is generally more labile than Al, resulting in an increase in $^{27}Al/^{24}Mg$ at fixed $\delta^{26}Mg^*$ in Figure 19. Transition state theory predicts that leaching of Mg would likely be more efficacious for the light Mg isotope and a mass-dependent fractionation to higher $\delta^{25}Mg$ and $\delta^{26}Mg$ values at fixed $\delta^{26}Mg^*$ should occur as the isotopically lighter Mg is carried away.

On the ^{26}Al-$^{26}Mg^*$ evolution diagram analyses of unaltered material define a line with a slope corresponding to an initial $^{26}Al/^{27}Al$ of 6.3×10^{-5} and an intercept of $\delta^{26}Mg^* = 0.009$ (Fig. 19). The intercept is effectively zero despite the fact that the regression line was not forced to pass through the origin. The initial $^{26}Al/^{27}Al$, or $(^{26}Al/^{27}Al)^o$, of 6.3×10^{-5} defined by the unaltered minerals is identical to that suggested by the single acid-digestion MC-ICPMS measurement of a bulk CAI from Allende (Table 1) (Galy et al. 2000). Both the laser ablation data for unaltered minerals and the bulk CAI datum yield higher initial $(^{26}Al/^{27}Al)$ values than the canonical value of 5×10^{-5} (MacPherson et al. 1995). The uncertainty in the slope permits a lower $(^{26}Al/^{27}Al)^o$ consistent with the canonical value but only if the intercept approaches 0.5‰ rather than zero (Fig. 19). A non-zero intercept implies a significant departure from normal Mg isotope ratios in the Solar System (Fig. 2), and there is little evidence to support such a large intercept given the uniformity of Solar System materials (e.g., Fig. 2). For this reason the higher slope is the preferred interpretation of the data in Figure 19. Evaluation of the significance of the higher $(^{26}Al/^{27}Al)^o$ will require numerous measurements in a wide variety of CAIs (Young et al. 2002a).

These first experiments demonstrate the viability of using laser ablation in combination with MC-ICPMS as a tool for measuring Mg isotope ratios in-situ in extraterrestrial materials. The advantages are high analytical precision combined with in-situ sampling on the microgram scale, independent measurements of both $\delta^{25}Mg$ and $\delta^{26}Mg$ at the 0.2‰ (2σ) level of precision, and negligible matrix effects in Mg-rich minerals (Young et al. 2002a). In this particular application, it was shown that with this new tool it will be possible to determine the causes of dispersion on the ^{26}Al-$^{26}Mg^*$ evolution diagram with less ambiguity than with other methods, aiding the interpretation of the data in terms of relative chronology.

Future studies should make use of the combination of rapid analysis time and high precision afforded by laser ablation in order to compile larger data sets for the myriad of different objects found in meteorites.

SUMMARY

The high precision with which Mg isotope ratios can be measured using MC-ICPMS opens up new opportunities for using Mg as a tracer in both terrestrial and extraterrestrial materials. A key advance is the ability to resolve kinetic from equilibrium mass-dependent fractionation processes. From these new data it appears that Mg in waters is related to mantle and crustal reservoirs of Mg by kinetic fractionation while Mg in carbonates is related in turn to the waters by equilibrium processes. Resolution of different fractionation laws is only possible for measurements of Mg in solution at present; laser ablation combined with MC-ICPMS (LA-MC-ICPMS) is not yet sufficiently precise to measure different fractionation laws.

Variability in Mg isotope ratios among chondritic meteorites and their constituents is dominated by mixing between a radiogenic CAI-like reservoir and a reservoir resembling ordinary chondrites. The mixing is evident in $\delta^{25}Mg$ and $\delta^{26}Mg$, Al/Mg, and $\Delta^{17}O$ values but

will require substantiation by collection of more MC-ICPMS Mg isotope data together with oxygen isotope and elemental compositions of bulk objects.

Laser ablation combined with LA-MC-ICPMS provides a new dimension to the analysis of Mg isotopes in calcium aluminum-rich inclusions from primitive meteorites. Dispersion in $^{26}Mg^*$-$^{27}Al/^{24}Mg$ evolution lines can be correlated with mass-dependent variations in $\delta^{25}Mg$ that distinguish open-system from closed-system processes. The ultimate product of such studies will be a better understanding of the chronological significance of variations in $^{26}Mg^*$ in these objects.

REFERENCES

Alexander CMOD (2003) Making CAIs and chondrules from CI dust in a canonical nebula. Lunar and Planetary Science Conference XXXIV:1391

Alexander CMOD, Grossman JN, Wang J, Zanda B, Bourot-Denise M, Hewins RH (2000) The lack of potassium-isotopic fractionation in Bishunpur chondrules. Meteor Planet Sci 35:859-868

Alexander CMOD, Wang J (2001) Iron isotopes in chondrules: implications for the role of evaporation during chondrule formation. Meteor Planet Sci 36**:**419-428

Cary EE, Wood RJ, Schwartz R (1990) Stable Mg isotopes as tracers using ICP-MS. J Micronutrient Anal 8(1):13-22

Catanzaro EJ, Murphy TJ, Garner EL, Shields WR (1966) Absolute isotopic abundance ratios and atomic weight of magnesium. J Res Natl Bur Stand 70A:453-458

Chang VT-C, Makishima A, Belshaw NS, O'Nions RK (2003) Purification of Mg from low-Mg biogenic carbonates from isotope ratio determination using multiple collector ICP-MS. J Anal At Spectrom 18: 296-301

Clayton RN, Hinton RW, Davis AM (1988) Isotopic variations in the rock-forming elements in meteorites. Philosoph Trans R Soc London, Ser A 325:483-501

Clayton RN, Mayeda TK (1977) Correlated oxygen and magnesium isotope anomalies in Allende inclusions, I: Oxygen. Geophys Res Lett 4(7):295-298

Clayton RN, Mayeda TK, Goswami JN, Olsen EJ (1991) Oxygen isotope studies of ordinary chondrites. Geochim Cosmochim Acta 55:2317-2337

Clayton RN, Mayeda TK (1999) Oxygen isotope studies of carbonaceous chondrites. Geochim Cosmochim Acta 63:2089-2103

Clayton RN, Onuma N, Grossman L, Mayeda TK (1977) Distribution of presolar component in Allende and other carbonaceous chondrites. Earth Planet Sci Lett 34:209-224

Davis AM, Hashimoto A, Clayton RN, Mayeda TK (1990) Isotope mass fractionation during evaporation of Mg_2SiO_4. Nature 347:655-658

Dombovari J, Becker JS, Dietze H-J (2000) Isotope ratio measurements of magnesium and determination of magnesium concentration by reverse isotope dilution technique on small amounts of ^{26}Mg-spiked nutrient solutions with inductively coupled plasma mass spectrometry. Int J Mass Spectrom 202:231-240

Fahey AJ, Goswami JN, McKeegan KD, Zinner E (1987) ^{26}Al, ^{244}Pu, ^{50}Ti, REE, and trace element abundances in hibonite grains from CM and CV meteorites. Geochim Cosmochim Acta 51(2):329-350

Galy A, Bar-Matthews M, Halicz L, O'Nions RK (2002) Mg isotopic composition of carbonate: insight from speleothem formation. Earth Planet Sci Lette 201:105-115

Galy A, Belshaw NS, Halicz L, O'Nions RK (2001) High-precision measurement of magnesium isotopes by multiple-collector inductively coupled plasma mass spectrometry. Int J Mass Spectrom 208:89-98

Galy A, O'Nions RK (2000) Is there a CHUR for Mg? Goldschmidt 2000, 424

Galy A, Yoffe O, Janney PE, Williams RW, Cloquet C, Alard O, Halicz L, Wadwha M, Hutcheon ID, Ramon E, Carignan J (2003) Magnesium isotopes heterogeneity of the isotopic standard SRM980 and new reference materials for magnesium-isotope-ratio measurements. J Anal At Spectrom 18:1352-1356

Galy A, Young ED, Ash RD, O'Nions RK (2000) The formation of chondrules at high gas pressures in the solar nebula. Science 290:1751-1753

Goswami JN, Srinivasan G, Ulyanov AA (1994) Ion microprobe studies of Efremovka CAIs: I. Magnesium isotope composition. Geochim Cosmochim Acta 58:431-447

Gray CM, Compston W (1974) Excess ^{26}Mg in the Allende meteorite. Nature 251:495-497

Gussone N, Eisenhauer A, Heuser A, Dietzel M, Bock B, Bohm F, Spero SJ, Lea DW, Bijma J, Nagler TF (2003) Model for kinetic effects on calcium isotope fractionation ($\delta^{44}Ca$) in inorganic aragonite and cultured planktonic foraminifera. Geochim Cosmochim Acta 67:1375-1382

Hsu W, Wasserburg GJ, Huss GR (2000) High time resolution by use of ^{26}Al chronometer in the multistage formation of a CAI. Earth Planet Sci Lett 182:15-29

Hulston JR, Thode HG (1965) Variations in the S^{33}, S^{34}, and S^{36} contents of meteorites and their relation to chemical and nuclear effects. J Geophys Res 70:3475-3484

Kennedy AF, Beckett JR, Edwards DA, Hutcheon ID (1997) Trace element disequilibria and magnesium isotope heterogeneity in 3655A: Evidence for a complex multi-stage evolution of a typical Allende type B1 CAI. Geochim Cosmochim Acta (7):1541-1561

Lee T, Papanastassiou DA (1974) Mg isotopic anomalies in the Allende meteorite and correlation with O and Sr effects. Geophys Res Lett 1:225-228

MacPherson GJ, Davis AM, Zinner EK (1995) The distribution of aluminum-26 in the early Solar System - a reappraisal. Meteoritics 30:365-386

Mahon KI (1996) The "new" York regression: application of an improved statistical method to geochemistry. Int Geol Rev 38:293-303

Matsuhisa J, Goldsmith JR, Clayton RN (1978) Mechanisms of hydrothermal crystallisation of quartz at 250 C and 15 kbar. Geochim Cosmochim Acta 42:173-182

McKinney CR, McCrea JM, Epstein S, Allen HA, Urey HC (1950) Improvements in mass spectrometers for the measurement of small differences in isotope abundance ratios. Rev Scientific Inst 21(8):724-730

Norman M, McCulloch M, O'Neill H, Brandon A (2004) Magnesium isotopes in the Earth, Moon, Mars, and Pallasite parent body: high precision analysis of olivine by laser ablation multi-collector ICPMS. Lunar and Planetary Science Conference XXXV:1447

Richter FM, Davis AM, Ebel DS, Hashimoto A (2002) Elemental and isotopic fractionation of type B calcium-aluminum-rich inclusions: Experiments, theoretical considerations, and constraints on their thermal evolution. Geochim Cosmochim Acta 66(3):521-540

Russell SS, Huss GR, Fahey AJ, Greenwood RC, Hutchison R, Wasserburg GJ (1998) An isotopic and petrologic study of calcium-aluminum-rich inclusions from CO3 meteorites. Geochim Cosmochim Acta 62(4):689-714

Sahijpal S, Goswami JN, Davis AM, Grossman L, Lewis RS (1998) A stellar origin for the short-lived nuclides in the early Solar System. Nature 391:559-560

Schmitt AD, Stille P, Vennemann T (2003) Variations of the ^{44}Ca/^{40}Ca ratio in seawater during the past 24 million years: evidence from δ^{44}Mg and δ^{18}O values of Miocene phosphates. Geochim Cosmochim Acta 67:2607-2614

Schramm DN, Tera F, Wasserburg GJ (1970) The isotopic abundance of ^{26}Mg and limits on ^{26}Al in the early solar system. Earth Planet Sci Lett 10(1):44-59

Wasserburg GJ, Lee T, Papanastassiou DA (1977) Correlated oxygen and magnesium isotopic anomalies in Allende inclusions: II. magnesium. J Geophys Res 4:299-302

Weston RE (1999) Anomalous or mass-independent isotope effects. Chemical Reviews 99:2115-2136

Young ED, Ash RD, Galy A, Belshaw NS (2002a) Mg isotope heterogeneity in the Allende meteorite measured by UV laser ablation-MC-ICPMS and comparisons with O isotopes. Geochim Cosmochim Acta 66(4): 683-698

Young ED, Galy A, Nagahara H (2002b) Kinetic and equilibrium mass-dependent isotope fractionation laws in nature and their geochemical and cosmochemical significance. Geochim Cosmochim Acta 66(6): 1095-1104

Zhu XK, Guo Y, O'Nions RK, Young ED, Ash RD (2001) Isotopic homogeneity of iron in the early solar nebula. Nature 412:311-313